Journal of Computational Physics 229 (2010) 3189–3213

Contents lists available at ScienceDirect

Journal of Computational Physics

journal homepage: www.elsevier.com/locate/jcp

On the use of flux limiters in the discrete ordinates method for 3D radiation calculations in absorbing and scattering media

William F. Godoy, Paul E. DesJardin *

Department of Mechanical and Aerospace Engineering, University at Buffalo, The State University of New York, Buffalo, NY 14260, USA

ARTICLE INFO

Article history:
Received 25 September 2008
Received in revised form 1 December 2009
Accepted 30 December 2009
Available online 11 January 2010

Keywords:
Radiative transfer equation (RTE)
Discrete ordinates method (DOM)
Flux limiters
TVD schemes
Radiation heat transfer
Non-homogeneous 3D media
Newton–Krylov GMRES

ABSTRACT

The application of flux limiters to the discrete ordinates method (DOM), S_N, for radiative transfer calculations is discussed and analyzed for 3D enclosures for cases in which the intensities are strongly coupled to each other such as: radiative equilibrium and scattering media. A Newton–Krylov iterative method (GMRES) solves the final systems of linear equations along with a domain decomposition strategy for parallel computation using message passing libraries in a distributed memory system. Ray effects due to angular discretization and errors due to domain decomposition are minimized until small variations are introduced by these effects in order to focus on the influence of flux limiters on errors due to spatial discretization, known as numerical diffusion, smearing or false scattering. Results are presented for the DOM-integrated quantities such as heat flux, irradiation and emission. A variety of flux limiters are compared to "exact" solutions available in the literature, such as the integral solution of the RTE for pure absorbing-emitting media and isotropic scattering cases and a Monte Carlo solution for a forward scattering case. Additionally, a non-homogeneous 3D enclosure is included to extend the use of flux limiters to more practical cases. The overall balance of convergence, accuracy, speed and stability using flux limiters is shown to be superior compared to step schemes for any test case.

1. Introduction

Since it was first proposed by Chandrasekhar [1], the discrete ordinates method (DOM) has enjoyed great popularity in the solution of the radiative transfer equation (RTE) [2]. Several improvements to the method were achieved by Lathrop and Carlson in their early work on neutron transport [3] and the solution of the Boltzmann equation [4]. The straightforward formulation of the method, consisting in breaking up the continuous angular intensity field into concentrated intensities at prescribed directions and weights, allows its application in many problems involving radiative transfer in multidimensional Cartesian coordinates, as done by Fiveland and Jamaluddin [5,6]. The downside of the DOM is the high computational resources required as the number of unknown intensities increases dramatically when a more refined discretization is applied. For an extensive review of the method and its applications the reader is referred to the chapter on the DOM in the book by Modest [2].

Two major drawbacks are present in the DOM: (i) ray effects, caused by the discretization of the angular intensity and (ii) numerical smearing (known also as false scattering or numerical diffusion) due to spatial discretization. These two problems had been studied by Chai et al. [7] and Coelho [8]. The latter analyzed the compensation between the two errors showing that mesh refinement would reduce numerical smearing but increases ray effects. To overcome numerical smearing Lathrop

* Corresponding author. Tel.: +1 716 645 1467; fax: +1 716 645 2883.
E-mail address: ped3@buffalo.edu (P.E. DesJardin).

0021-9991/$ - see front matter © 2010 Elsevier Inc. All rights reserved.
doi:10.1016/j.jcp.2009.12.037

and Carlson proposed the diamond scheme based on central differences [3] as an improvement to the first order (step) scheme. Although better accuracy is obtained for certain cases, the diamond scheme may become unstable producing negative intensities. Lathrop and Carlson recommended to replace these negative intensities by zero, hence introducing the idea of limiting intensity values. Fiveland [5] provides stability criteria for the diamond scheme when applied to pure absorbing and emitting media. In his formulation the cell size is a function of the corresponding directional cosine and the medium optical thickness, stating that beyond this limit oscillations will occur. Further improvements include the high order schemes applied by Jessee and Fiveland [9] in 3D enclosures and the modified discrete ordinates method (MDOM) developed by Ramankutty and Crosbie [10] to reduce ray effects in a 2D Cartesian grid. Moreover, the importance of reducing numerical smearing is addressed by Mihalas and Klein [11], and more recently by Ayranci and Selçuk [12], who found in their work on the method of lines (MOL) for transient radiative transfer that errors due to numerical smearing become unacceptable for a moving media framework as in most practical applications (*i.e.*, fires, explosions, furnaces, the atmosphere).

Flux limiters are part of the high order total variation diminishing (TVD) techniques originally developed for the solution of fluid mechanics equations [13,14] to satisfy certain conditions such as monotonicity and the introduction of high order bounded (non-oscillatory) schemes [15,16]. The application of flux limiters on the DOM for radiative problems has gained popularity in recent years as it combines the robust characteristic of first order schemes (step) at discontinuities and the accuracy of higher order schemes (*e.g.* diamond scheme [3]) for relatively smooth media. Through the use of flux limiters, face cell intensities are related to cell averaged intensities by a non-linear relationship of three adjacent values, two upstreams and one downstream, increasing the accuracy between a first and second order scheme. Balsara [17] reviews the different basic methods of this technique along with the application of multigrid methods on multidimensional radiative transfer for 2D homogeneous media with constant source terms. A truly multidimensional discretization scheme [18], that follows the direction of propagation instead of that of the computational mesh (dimension by dimension), was proposed by Coelho [19,20]. His work on bounded skewed schemes for the DOM in 2D homogeneous cases shows that a truly multidimensional discretization is not always attractive due to slow convergence rates and nearly no gains in optically thick media therefore the improved accuracy does not compensate the programming effort for this method.

The final system of equations are solved using a Newton–Krylov iterative method (GMRES) [21]. It was stated by Balsara [17] that a Newton–Krylov method may be preferable than a Gauss–Seidel method since it avoids operator splitting between the first order derivatives and the source terms, degrading convergence for cases where the intensities are strongly coupled to each other not resulting in a diagonal dominant Jacobian in a Newton formulation. With the aim of parallel computational resources and message passing libraries [22] in the recent decade, it is possible to carry out radiative calculations for large 3D domains [23] to allow for more refined meshes and a higher number of S_N ordinates. A domain decomposition parallelization in a distributed memory system is used in the present study as in [23].

In the present work, a comparison on the application of different flux limiters in the DOM for 3D Cartesian enclosures is shown for radiative transfer cases in which the intensities are strongly coupled to each other through the source term. Three dimensional, non-homogeneous, non-isothermal and scattering media are of particular interest since a generalization of the DOM must account for all these characteristics. Also, the number of S_N-ordinates for the whole sphere in 3D, $N(N+2)$, is much larger than in 2D and 1D cases, $N(N+2)/2$ and $2N$, respectively. Therefore, 3D problems differ from 2D and 1D when the DOM is applied to the angular discretization of the intensities. Three test cases are presented including: (i) pure absorbing and emitting media in radiative equilibrium, (ii) pure isotropic and forward scattering with constant temperature field, and (iii) non-homogeneous, non-isothermal, absorbing, emitting and scattering media in a constant temperature field.

Additionally, the volume average intensities for the scattering terms in the RTE are calculated from a linear combination of the face intensities entering the control rather than taking the cell centered intensities, yielding more accurate results in a problem with a strong scattering medium, as shown in the results section. A discussion is presented for the most important numerical aspects such as: stability, convergence, computational time and memory storage. The accuracy of different limiters is compared with "exact" results available in the literature such as the integral solution of the RTE [24] for pure absorbing-emitting media in radiative equilibrium in case (i) and isotropic scattering in case (ii), whereas the Monte Carlo method [25] is shown to compare results in the forward scattering case. Finally, average computational times and overall convergence history for thin and thick media are shown for case (iii) that includes a 3D non-homogeneous problem, as in most practical applications, for which exact answers using a Monte Carlo method may become impractical. To the authors' best knowledge the present calculations have not been carried out to evaluate the performance of different flux limiters in the DOM in 3D media using a multidomain parallel computation.

2. Mathematical formulation

2.1. Radiative transfer equation

The spectral radiative transfer equation in a participating medium where the wavelengths do not interact with each other is given by [2]:

$$\vec{s}\cdot\vec{\nabla}I_\eta = k_\eta I_{b\eta} - \beta_\eta I_\eta + \frac{\sigma_\eta}{4\pi}\int_{4\pi} I_\eta \Phi_\eta(\vec{s}',\vec{s})\,d\Omega' \tag{1}$$

where I_η is the spectral radiative intensity which depends on the path-length (s), absorption (k_η), scattering (σ_η) and total extinction ($\beta_\eta = k_\eta + \sigma_\eta$) coefficients along with the scattering phase function (Φ_η), Ω' is an arbitrary solid angle in the $\vec{s}'$ direction and $I_{b\eta}$ represents the blackbody intensity and depends on the local temperature of the medium.

The boundary conditions for the RTE for diffuse emissive and reflective walls are given by:

$$I_{w\eta} = \epsilon_\eta I_{b\eta} + \frac{\rho_\eta}{\pi} \int_{\vec{s}\cdot\vec{e}_w<0} |\vec{s}\cdot\vec{e}_w| I_\eta \, d\Omega' \tag{2}$$

where $I_{w\eta}$ is the intensity coming out from the wall, ϵ_η and $\rho_\eta (\epsilon_\eta + \rho_\eta = 1)$ are the diffuse surface emissivity and reflectivity, respectively. $I_{b\eta}$ is the surface blackbody intensity that depends on the wall temperature, T_w, and $\vec{e}_w$ represents the unit vector normal to the wall surface which in Cartesian coordinates becomes the standard basis vectors for 3D domains $(\vec{i},\vec{j},\vec{k})$.

The net radiative heat flux in the $\vec{s}$ direction, $\vec{q}(\vec{s})$, the local incident radiation, G, and the local heat flux divergence, $\vec{\nabla}\cdot\vec{q}$, are obtained from the solution of the intensity field, I_η, in Eqs. (1) and (2) by:

$$\vec{q}(\vec{s}) = \int_0^\infty \int_{4\pi} I_\eta \vec{s} \, d\Omega' \, d\eta \tag{3a}$$

$$G = \int_0^\infty \int_{4\pi} I_\eta \, d\Omega' \, d\eta \tag{3b}$$

$$\vec{\nabla}\cdot\vec{q} = \int_0^\infty k_\eta (4\pi I_{b\eta} - G_\eta) \, d\eta \tag{3c}$$

Near exact solutions of the RTE exist for 3D media, among these are the Monte Carlo [26] and the zone method [27]. Additionally, exact integral expressions for the solution of the RTE are given by Crosbie and Schrenker [24] for 3D media in radiative equilibrium and constant temperature cases for either pure absorbing-emitting or isotropic scattering media. The main disadvantages of all of these methods are their prohibitive computational costs to reach a near exact solution of the RTE and, except for the Monte Carlo method due to its statistical nature, the fact that they can only be applied to certain configurations. Therefore, the need to search for more practical alternatives for which computational costs are reduced without compromising accuracy is required.

3. Methods of solution

3.1. Angular discretization using the discrete ordinates method (DOM)

The basic idea of the DOM is to break up the continuous intensity into prefixed ordinates in which the intensity is concentrated [1]. To focus on the method of solution of the RTE, the spectral dependence is omitted for the rest of the manuscript and only the numerical aspects are included since non-gray media problems with non-interacting wavelengths can be solved applying these methods independently to each spectral region. Applying angular discretization, Eqs. (1) and (2) are transformed into a set of partial differential equations when replacing the integrals by summations of weighted factors. In a 3D Cartesian domain,

$$\xi_m \frac{\partial I_m}{\partial x} + \eta_m \frac{\partial I_m}{\partial y} + \mu_m \frac{\partial I_m}{\partial z} + \beta I_m = k I_b + \frac{\sigma}{4\pi} \sum_{n=1}^{N(N+2)} w_n \Phi_{nm} I_n \tag{4a}$$

$$I_{m,w} = \epsilon I_{b,w} + \frac{\rho}{\pi} \sum_{\vec{e}_w\cdot\vec{s}_n<0} w_n |\vec{e}_w \cdot \vec{s}_n| I_n \tag{4b}$$

where ξ, η and μ are the cosines of the selected m ordinate direction with respect to the x, y and z axis, respectively, as shown in Fig. 1(a). I_m represents the intensity in the m direction. The integral term in the right hand side of Eq. (4a) is replaced by the summation of the contribution due to in-scattering from the intensity in the arbitrary n direction, I_n, into the m ordinate. The quantity w_n is the weight assigned to the n ordinate direction. In the present work, the S_N quadrature sets given by Balsara [17] are applied. In his work, the weights and quadratures originally provided by Fiveland [28] are slightly modified to preserve up to 20 moments. Fiveland proposed a level symmetric hybrid (LSH) formulation to obtain the quadratures preserving odd and even moments being superior to conventional level symmetric even (LSE) ordinates [3]. As an example, the S_8 LSH quadrature given by Balsara preserves the first 8 moments up to 0.47% accuracy and up to 7.0% for the first 15 moments. Fiveland also provides quadratures to preserve the conservation of the half range moment which is important for calculating wall and cell face heat fluxes.

A drawback in the use of the DOM is the re-normalization of the phase scattering function (PSF) in strong forward anisotropic scattering media. This matter has been recently analyzed and discussed by Boulet et al. [25] when comparing the DOM with finite volume methods (FVM) for acute forward scattering cases. They concluded that re-normalization of the PSF from Mie theory is not desirable as it loses the physics of the problem leading to larger errors, instead they prefer the delta approximation given by Wiscombe [29,30]. In this work, the Henyey–Greenstein approximation [31] is used along with re-normalization as the forward peak can be dramatically overestimated leading to large errors in the calculation of heat fluxes.

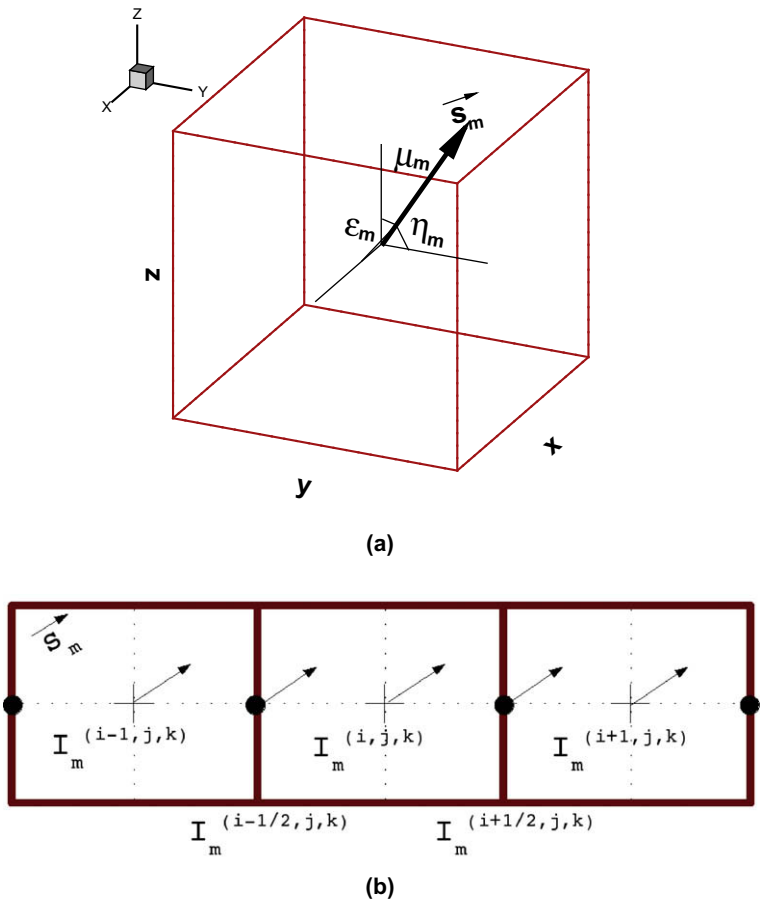

Fig. 1. Discretization strategy for the RTE intensities. (a) Angular discretization showing a 3D Cartesian domain and the cosine orientations of a single ordinate, m, and (b) finite volume spatial discretization strategy showing the upstream, $I_m^{(i-1,j,k)}$, central, $I_m^{(i,j,k)}$, and downstream, $I_m^{(i+1,j,k)}$, cell centered intensities and the corresponding face intensities, $I_m^{(i-1/2,j,k)}$ and $I_m^{(i+1/2,j,k)}$, for the central cell, (i,j,k).

As the main interest in most practical 3D applications are the integrated quantities over the whole sphere due to radiative energy conservation, Eqs. (3a) and (3b) are transformed due to the DOM for a specific location (x,y,z) as:

$$\vec{q}(\vec{s}) = \sum_{n=1}^{N(N+2)} w_n I_n(\vec{s}_n \cdot \vec{s})\vec{s} \tag{5a}$$

$$G = \sum_{n=1}^{N(N+2)} w_n I_n \tag{5b}$$

where N represents the order of approximation in the angular discretization and the number of ordinate directions over the eight octants of the whole sphere (4π) is $N(N+2)$, and I_n is the intensity in a specific direction as shown in Fig. 1(a) for a single direction $\vec{s}_n$ defined by its directional cosines (ξ_n, η_n, μ_n). So for the S_4, S_6, S_8, S_{10} and S_{12} quadratures the number of directions that represent the intensity field at each location are 24, 48, 80, 120 and 168, respectively.

3.2. Finite volume discretization using flux limiters for the DOM in the RTE

As pointed out by Modest [2] it is more common to employ the finite-volume approach for the spatial discretization of the RTE proposed by Lathrop and Carlson [3,4]. The control volumes are usually taken small enough so the radiative properties of the media, β, k, σ, Φ_{nm} and I_b are considered constant inside the volume allowing for homogenization of the smaller scales. Taking the ordinate directions as fixed, Eqs. (4a) and (4b) are discretized as follows,

$$\xi_m \int_{\Delta V} \frac{\partial I_m}{\partial x}\, dV + \eta_m \int_{\Delta V} \frac{\partial I_m}{\partial y}\, dV + \mu_m \int_{\Delta V} \frac{\partial I_m}{\partial z}\, dV + \beta \int_{\Delta V} I_m\, dV = kI_b \int_{\Delta V} dV + \frac{\sigma}{4\pi} \sum_{n=1}^{N(N+2)} w_n \Phi_{nm} \int_{\Delta V} I_n\, dV \tag{6a}$$

$$\int_{\Delta A_w} I_{m,w}\, dA_w = \epsilon I_{b,w} \int_{\Delta A_w} dA_w + \frac{\rho}{\pi} \sum_{\vec{e}_w \cdot \vec{s}_n < 0} w_n |\vec{e}_w \cdot \vec{s}_n| \int_{\Delta A_w} I_n\, dA_w. \tag{6b}$$

In general, for the x direction in a multidimensional system [2],

$$\int_V \frac{\partial I_m}{\partial x}\, dV \simeq I_m^{(i\pm 1/2,j,k)} A_x^{(i\pm 1/2,j,k)} - I_m^{(i\mp 1/2,j,k)} A_x^{(i\mp 1/2,j,k)}. \tag{7}$$

The selection of the upper index sign in Eq. (7) depends on the alignment of the "m" direction with respect to the coordinate axis in question. The upper signs (+ and −) are used for the x axis if $\vec{s}_m \cdot \vec{e}_x > 0$, whereas the lower signs (− and +) are selected if $\vec{s}_m \cdot \vec{e}_x < 0$. This also applies to the other directions, y and z. Since this work is developed for regular 3D Cartesian domains the cell face areas along one direction are constant (*e.g.* $A_x = \Delta y \Delta z = constant$) therefore, after dividing by a constant volume element ($\Delta V = \Delta x \Delta y \Delta z$), the RTE and boundary conditions have the following form,

$$|\xi_m| \frac{I_m^{(i\pm 1/2,j,k)} - I_m^{(i\mp 1/2,j,k)}}{\Delta x} + |\eta_m| \frac{I_m^{(i,j\pm 1/2,k)} - I_m^{(i,j\mp 1/2,k)}}{\Delta y} + |\mu_m| \frac{I_m^{(i,j,k\pm 1/2)} - I_m^{(i,j,k\mp 1/2)}}{\Delta z} + \beta I_{p,m}^{(i,j,k)}$$
$$= kI_b^{(i,j,k)} + \frac{\sigma}{4\pi} \sum_{n=1}^{N(N+2)} w_n \Phi_{nm} I_{p,n}^{(i,j,k)} \tag{8a}$$

$$I_{m,w} = \epsilon I_{b,w} + \frac{\rho}{\pi} \sum_{\vec{e}_w \cdot \vec{s}_n < 0} w_n |\vec{e}_w \cdot \vec{s}_n| I_{pw,n}^{(i,j,k)} \tag{8b}$$

where the absolute value is introduced for the directional cosines keeping the sign criteria as explained above and the terms $I_{p,m}$ and $I_{p,n}$ are the volume average intensities for the m and n directions, respectively. They are defined as $I_{p,m} = \int_{\Delta V} I_m\, dV / \Delta V$. Typically this term is chosen to be a linear relationship between the in-coming and out-coming intensities at the cell faces [2] resulting in the so-called step and diamond schemes [3,4]. In the present work, it is proposed that the self-extinction term $I_{p,m}$ and the in-scattering term $I_{p,n}$ result from applying a linear relationship of the incoming intensities on the control volume, rather that including also the out-coming intensities as in the diamond scheme. This fact is shown in Fig. 2 for a schematic 2D representation of the incoming intensities from the upstream faces of the control volume. Extension to a 3D domain is straightforward therefore, $I_{p,m}$ is obtained as follows,

$$I_{p,m}^{(i,j,k)} = \frac{I_m^{(i\mp 1/2,j,k)} A_x^{(i\mp 1/2,j,k)} + I_m^{(i,j\mp 1/2,k)} A_y^{(i,j\mp 1/2,k)} + I_m^{(i,j,k\mp 1/2)} A_z^{(i,j,k\mp 1/2)}}{A_x^{(i\mp 1/2,j,k)} + A_y^{(i,j\mp 1/2,k)} + A_z^{(i,j,k\mp 1/2)}} \tag{9}$$

In a 3D Cartesian system where the control volumes are cubes and considering the discretization is similar on each direction, $\Delta x = \Delta y = \Delta z$, the factor of 3 takes place in Eq. (9) being $I_{p,m}^{(i,j,k)}$ the arithmetic average of the incoming intensities. In general, $A_x = \Delta y \Delta z$, $A_y = \Delta x \Delta z$ and $A_z = \Delta x \Delta y$, and Eq. (9) must be solved explicitly. The same concept must apply for $I_{p,n}^{(i,j,k)}$ since n is a dummy variable in the in-scattering term of the discretized RTE in Eq. (8a). The motivation for applying this formulation is the fact that scattering and absorption coefficients are local properties defined in a linear sense with units of L^{-1}. There is a

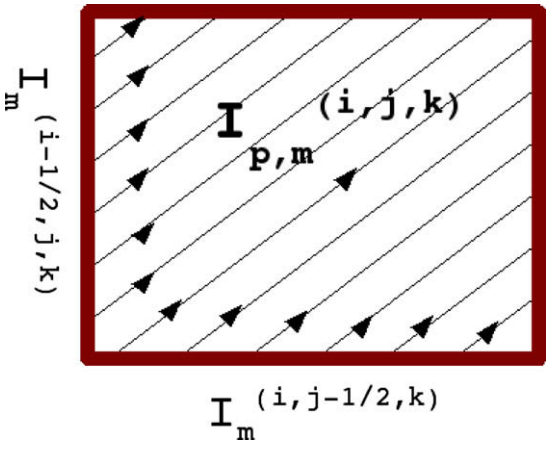

Fig. 2. Schematic 2D representation for the volume average intensity $I_{p,m}^{(i,j,k)}$ resulting from a linear relationship of the incoming upstream intensities at the cell faces, $I_m^{(i-1/2,j,k)}$ and $I_m^{(i,j-1/2,k)}$.

certain length for which scattering and absorption effects develop along the medium, being the incoming intensities to the control volume the ones affected rather than cell centered intensities.

Flux limiters relate cell face intensities to three cell average intensities of the vicinity for the same angular and spatial direction in order to reduce the number of unknowns in the total system of equations. As shown in Fig. 1(b), one upstream, one central and one downstream intensities are related to the face intensity in the x direction through [32,17],

$$I_m^{(i\pm 1/2,j,k)} = I_m^{(i,j,k)} + \frac{\Psi_m^{(i)}(r_m)}{2}\left(I_m^{(i,j,k)} - I_m^{(i\mp 1,j,k)}\right) \tag{10a}$$

$$r_m = \frac{I_m^{(i\pm 1,j,k)} - I_m^{(i,j,k)}}{I_m^{(i,j,k)} - I_m^{(i\mp 1,j,k)}} \tag{10b}$$

where the superscripts $(i \pm 1, j, k)$ and $(i \mp 1, j, k)$ indicate the downstream and upstream cells with respect to the cell center location, (i, j, k), respectively. $\Psi_m^{(i)}$ is the flux limiter for the x direction, which is a non-linear function of the ratio r_m given by the downstream, central and upstream cell average intensities defined with respect to the cell center. Flux limiters and their derivatives are bounded to certain values such that in limiting situations they recover first and higher order spatial accuracy ($0 \leqslant \Psi \leqslant 2$ and $0 \leqslant d\Psi/dr \leqslant 2$).

Applying Eq. (10a) into the discretized RTE in Eq. (4a), the spatial partial derivative in the x direction is transformed as,

$$I_m^{(i\pm 1/2,j,k)} - I_m^{(i\mp 1/2,j,k)} = I_m^{(i,j,k)} - I_m^{(i\mp 1,j,k)} + \frac{\Psi_m^{(i)}}{2}\left[I_m^{(i,j,k)} - I_m^{(i\mp 1,j,k)}\right] + \frac{\Psi_m^{(i\mp 1)}}{2}\left[I_m^{(i\mp 2,j,k)} - I_m^{(i\mp 1,j,k)}\right] \tag{11a}$$

where $\Psi_m^{(i)}$ and $\Psi_m^{(i\mp 1)}$ represent the flux limiters in the x direction at the central, (i, j, k), and upstream, $(i \mp 1, j, k)$, cells, respectively. It is seen from Eq. (11a) that the spatial derivative of I_m in the RTE is expressed as a first order term and two "anti-diffusion" terms associated with the inclusion of a flux limiter formulation. In the limit when $\Psi_m^{(i)} = \Psi_m^{(i\mp 1)} = 0$ a first order formulation is recovered for a specific direction, whereas for $\Psi_m^{(i)} = \Psi_m^{(i\mp 1)} = 2$ the right hand side of Eq. (11a) is

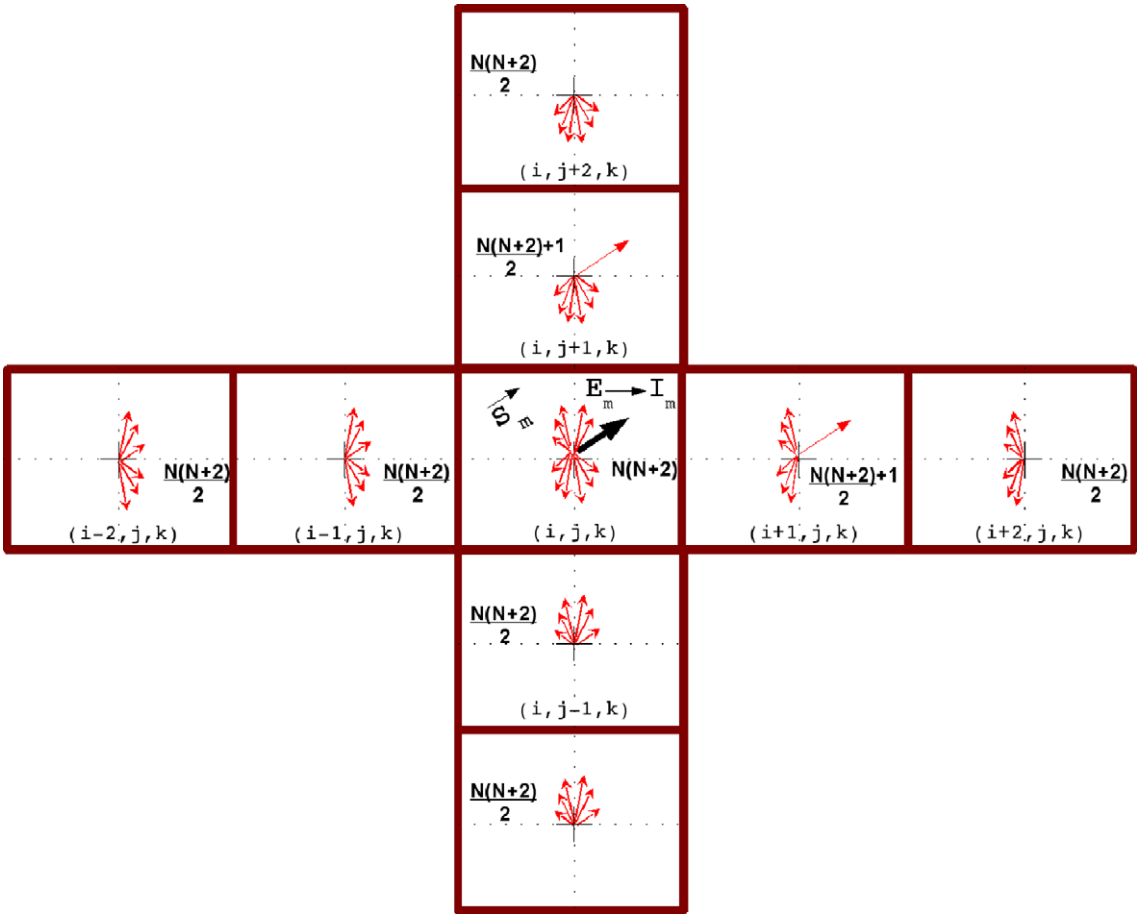

Fig. 3. Schematic 2D representation for the total number of cell centered intensities involved in the error function from Eq. (13a) in the upstream and downstream cells.

equal to $2I_m^{(i,j,k)} - 3I_m^{(i\mp1,j,k)} + 1I_m^{(i\mp2,j,k)}$ recalling a second order upwind scheme. Therefore, the first order stability characteristic is recovered for a specific direction at discontinuities where $\Psi_m = 0$ and a central scheme is applied at smooth regions, thus the inclusion of flux limiters results in a hybrid combination of the two.

A variety of flux limiters that are used in this work are given in Appendix A and classified as symmetric and non-symmetric. The symmetric limiters used in this work as given in [32] are: van Leer, van Albada, minmod (Roe), superbee (Roe), β-limiters (Sweby), monotonized central MC (van Leer), Ospre (Waterson and Deconinck), UMIST (Lien and Leschziner), whereas the non-symmetric limiters are: Chakravarthy-Osher and Koren.

For a 3D Cartesian problem with six boundaries the value of the total unknowns is given as,

$$M = N(N+2)[n_x n_y n_z + n_x n_y + n_x n_z + n_y n_z] \tag{12}$$

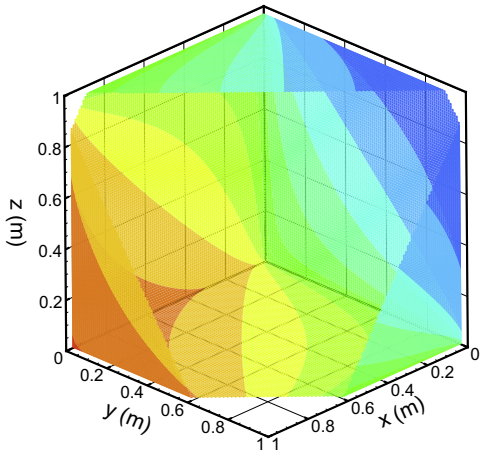

where M is the total number of unknown intensities, N refers to the S_N quadrature used, n_x, n_y and n_z are the number of cell volumes in the x, y and z directions, respectively. The factor $n_x n_y n_z$ appears due to the cell intensities inside the medium while for reflective boundaries each wall provides half of the numbers given in the rest of the right hand side terms (*i.e.*, the wall at $z = 0$ provides $N(N+2)[n_x n_y/2]$ unknowns). Therefore, intensities at the reflective boundaries are iterated along with the rest of the intensities in the medium rather that being taken from previous iterations. For enclosures with black walls the number of unknowns is reduced to $M = N(N+2)[n_x n_y n_z]$. It is important to mention that the number of total unknown intensities, M, depends on the total number of cells, the order of the S_N approximation and the boundary type only and not by the functional form of different spatial discretizations through the use of flux limiters.

3.3. Newton–Krylov GMRES solution

In order to solve the system of equations for the intensity field, a Newton–Krylov method is applied by first forming the error functions for each unknown intensity and then taking the partial derivatives to obtain the Jacobian matrix. The motivation for using Newton–Krylov methods, rather than other iterative methods such as Gauss–Seidel, is explained by Balsara

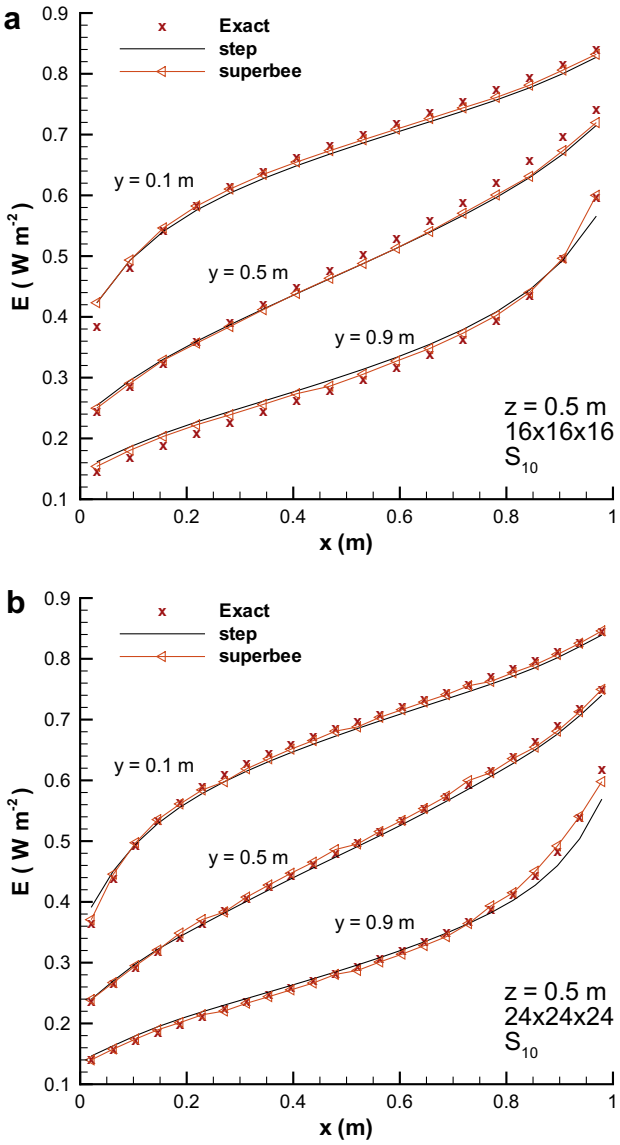

Fig. 6. Case 1: Comparison between the exact solution and the step and superbee limiter schemes using a S_{10} quadrature for the medium emission, E, in radiative equilibrium. Results are shown at the $z = 0.5$ m plane and three different locations in the y direction using two mesh resolutions: (a) $16 \times 16 \times 16$ and (b) $24 \times 24 \times 24$.

[17]. In scattering and radiative equilibrium problems the diagonal dominance of the problem is not guaranteed and therefore slow convergence is expected from a Gauss–Seidel solution, thus requiring acceleration methods [33]. A Newton–Krylov method offers a more general formulation of the iterative solution since no operator splitting is introduced for the source terms which is proven to slow down convergence in non-homogeneous, scattering and optically thick media cases requiring acceleration methods that increase programming and computational times [17,33].

An initial guess of the intensity field is obtained considering a pure absorbing medium with black walls. Iterations of the matrix solution are carried until a convergence criterion is achieved. From the previous section, the RTE and boundary conditions are transformed into a set of algebraic equations through angular and spatial discretization. In a Newton-type formulation the corresponding error functions for each unknown intensity are obtained applying Eq. (11a) on Eqs. (8a) and (8b). Resulting,

$$E_m^{(i,j,k)} = \frac{|\xi_m|}{\Delta x}\left[I_m^{(i,j,k)} - I_m^{(i\mp1,j,k)} + \frac{\Psi_m^{(i)}}{2}\left(I_m^{(i,j,k)} - I_m^{(i\mp1,j,k)}\right) - \frac{\Psi_m^{(i\mp1)}}{2}\left(I_m^{(i\mp1,j,k)} - I_m^{(i\mp2,j,k)}\right)\right]$$
$$+ \frac{|\eta_m|}{\Delta y}\left[I_m^{(i,j,k)} - I_m^{(i,j\mp1,k)} + \frac{\Psi_m^{(j)}}{2}\left(I_m^{(i,j,k)} - I_m^{(i,j\mp1,k)}\right) - \frac{\Psi_m^{(j\mp1)}}{2}\left(I_m^{(i,j\mp1,k)} - I_m^{(i,j\mp2,k)}\right)\right]$$
$$+ \frac{|\mu_m|}{\Delta z}\left[I_m^{(i,j,k)} - I_m^{(i,j,k\mp1)} + \frac{\Psi_m^{(k)}}{2}\left(I_m^{(i,j,k)} - I_m^{(i,j,k\mp1)}\right) - \frac{\Psi_m^{(k\mp1)}}{2}\left(I_m^{(i,j,k\mp1)} - I_m^{(i,j,k\mp2)}\right)\right] + \beta I_{p,m}^{(i,j,k)} - kI_b^{(i,j,k)} - \frac{\sigma}{4\pi}\sum_{n=1}^{N(N+2)} w_n \Phi_{nm} I_{p,n}^{(i,j,k)} \tag{13a}$$

$$E_{m,w} = I_{m,\mathrm{w}} - \epsilon I_{b,\mathrm{w}} - \frac{\rho}{\pi}\sum_{\vec{e}_\mathrm{w}\cdot\vec{s}_n<0} w_n |\vec{e}_\mathrm{w}\cdot\vec{s}_n| I_{pw,n}^{(i,j,k)}. \tag{13b}$$

To obtain an initial guess for the intensity field, black boundaries and an absorbing-emitting medium are assumed. For only this initial guess, $I_{p,m}^{(i,j,k)}$ is assumed to be equal to $I_m^{(i,j,k)}$ at every cell and only a single sweep, starting at the "known" intensities at the boundaries, is necessary for each decoupled intensity resulting in the following explicit expression for $I_m^{(i,j,k)}$,

$$I_m^{(i,j,k)} = \frac{kI_b + \frac{\xi_m}{\Delta x}\left(1+\frac{\Psi_m^{(i)}}{2}\right)I_m^{(i\mp1/2,j,k)} + \frac{\eta_m}{\Delta y}\left(1+\frac{\Psi_m^{(j)}}{2}\right)I_m^{(i,j\mp1/2,k)} + \frac{\mu_m}{\Delta z}\left(1+\frac{\Psi_m^{(k)}}{2}\right)I_m^{(i,j,k\mp1/2)}}{k + \frac{\xi_m}{\Delta x}\left(1+\frac{\Psi_m^{(i)}}{2}\right) + \frac{\eta_m}{\Delta y}\left(1+\frac{\Psi_m^{(j)}}{2}\right) + \frac{\mu_m}{\Delta z}\left(1+\frac{\Psi_m^{(k)}}{2}\right)} \tag{14}$$

All flux limiters are initially set to zero in Eq. (14) to obtain a guessed value for $I_m^{(i,j,k)}$, starting from the "known" intensities at the boundaries. Having the intensity guess, the limiters are recalculated and therefore the new $I_m^{(i,j,k)}$ values are obtained based on the non-linear limiters analogous to a predictor–corrector procedure [32].

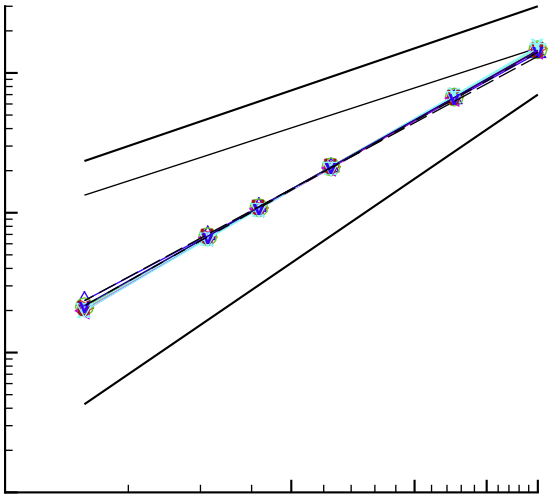

Once an initial guess is determined a Newton's method is used to solve the equations for the coupled intensities,

$$\frac{\partial E_m}{\partial I_n}\delta I_n = -E_m \tag{15a}$$

$$I_n^{p+1} = I_n^p + \delta I_n^p \tag{15b}$$

where the superscript p indicates the iteration number for which a Newton–Krylov solver is used. For completeness, the expressions of the first partial derivatives that form the Jacobian matrix in Eq. (15a) are given in Appendix B for the x direction. The derivatives for the other directions are obtained in an analogous way. If the iterative solution convergences, it is expected that $|\delta I_n^{p+1}| < |\delta I_n^p|$and, for this work, the convergence history is plotted for each limiter based upon the L_1 norm for the total number of intensities,

$$L_1 = \frac{\sum_{n=1}^{M}\left|\frac{\delta I_n^p}{I_n}\right|}{M} \tag{16}$$

To analyze mesh convergence the total average error of any integrated quantity along the entire medium is defined as,

$$L_E = \frac{\sum_{i=1}^{n_x}\sum_{i=1}^{n_y}\sum_{i=1}^{n_z}\left|\frac{E_{exact}-E_{DOM}}{E_{exact}}\right|}{n_x n_y n_z} \tag{17}$$

where E represents the emission, irradiation or heat flux.

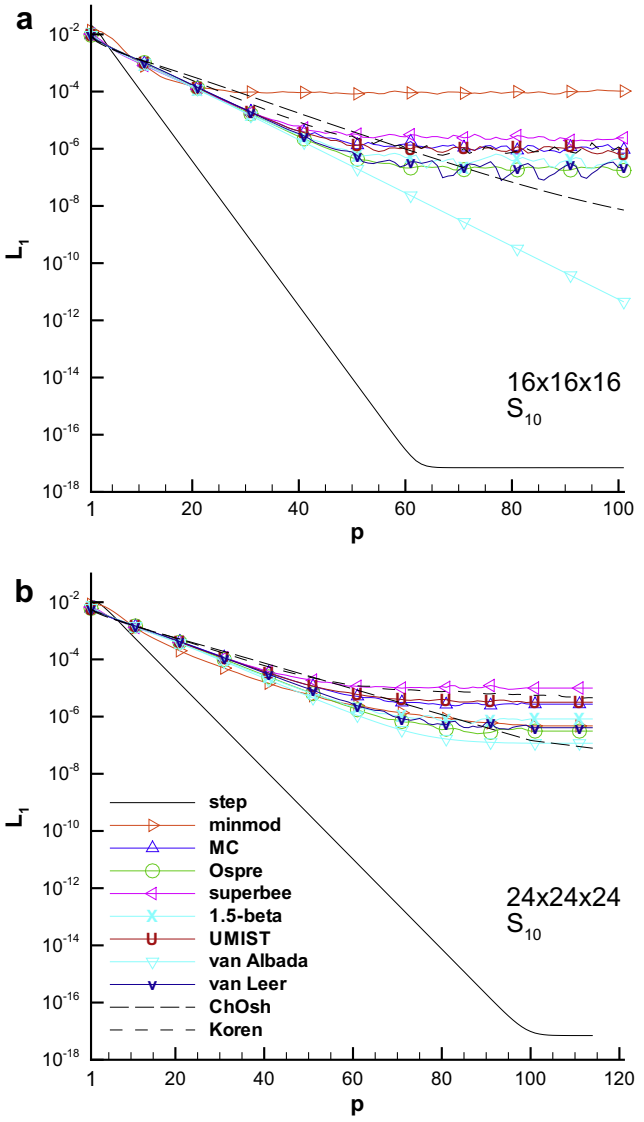

Fig. 8. Case 1: Convergence history of the step scheme and different limiters for the L_1 norm as a function of Newton iterations, p, using a GMRES(15) solution for (a) a $16 \times 16 \times 16$ and (b) a $24 \times 24 \times 24$ meshes.

Balsara [17] found that a general minimum residual method (GMRES) [21] shows a better performance when a Krylov subspace size of 15 is used in two restarted iterations instead of one for a Krylov subspace size of 30. This number is proportional to the memory required in solving the system and in general a greater value for the subspace size provides faster convergence at the expense of high memory storage. Since many systems have to be solved many times, large memory requirements exist when the explicit Jacobian is stored. The value of 15 for the Krylov subspace is used in the GMRES routine provided by the package Matrix Toolkits for Java (MTJ) [34] which is based on the well-known Fortran packages BLAS [35] and LAPACK [36] therefore convergence and memory storage are balanced. For a more detailed explanation on the GMRES method the reader is referred to the textbook of Saad [37]. Another alternative of potential use is the Jacobian free Newton–Krylov method for which its application to different areas has been extensively reviewed by Knoll and Keyes [38]. The memory requirements are significantly reduced at the expense of adding programming and computational times, although this alternative is out-of-scope in of the present work.

The inclusion of flux limiters in the solution of Eq. (4a) makes the Jacobian system large and sparse as the error function depends on $7N(N+2)+3$ intensities located at neighboring cells, in contrast to a step or diamond formulation where only $4N(N+2)+3$ variables are required due to the central intensities and one upstream intensity on each direction. Fig. 3 shows

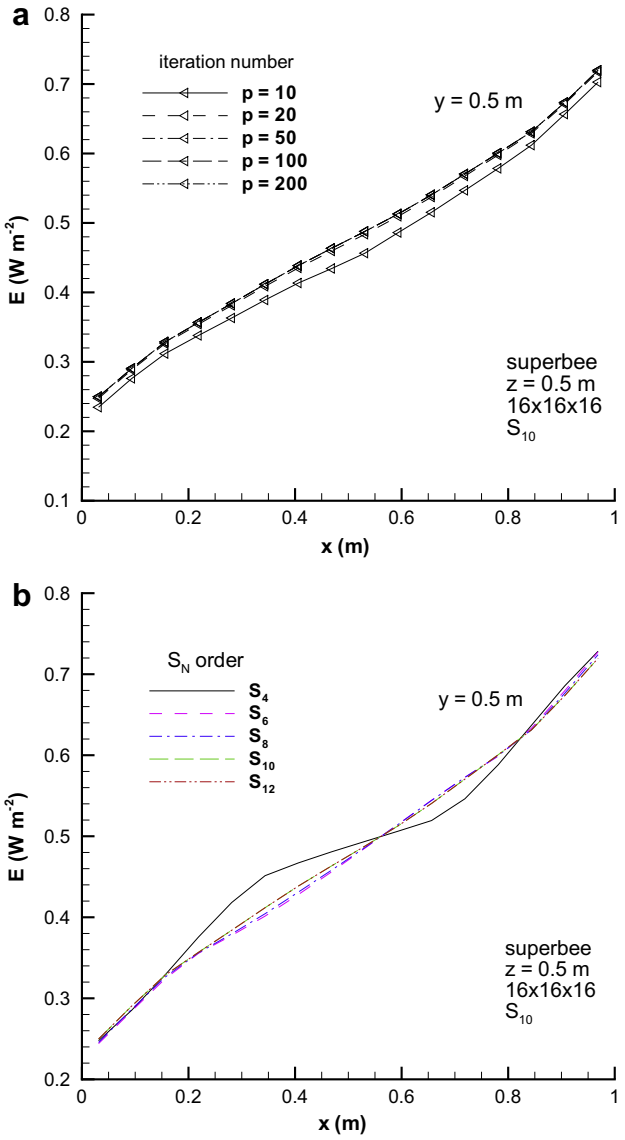

Fig. 9. Case 1: Emission along the medium in radiative equilibrium, E, for the superbee limiter on a $16 \times 16 \times 16$ mesh. Results show the convergence of E as a function of (a) the number of Newton iterations, p, and (b) S_N quadrature order.

a schematic 2D representation of the intensities that contribute to the error function in Eq. (13a) for which the contribution comes from $2N(N+2)+1$ intensities on each direction. Multiplying this factor by the number of directions, 3, and adding the central intensities $N(N+2)$ results in the factor $7N(N+2)+3$. This number is reduced at the nodes near the boundaries where the limiters are zero.

The fact of obtaining a large and sparse Jacobian with the introduction of flux limiters results in a slower convergence rate and therefore more number of iterations are required to achieve a certain convergence criterion. The advantage is that neither accuracy nor stability is compromised as in the step and diamond schemes, respectively. Memory storage is critical when a Newton method is used where the explicit Jacobian must be stored in an optimal way. Therefore, only the non-zero elements and their locations are processed so instead of storing $M \times M$ numbers, from Eq. (12), only the non-zero elements, $M[7N(N+2)+3]$, are stored along with their indices location in the Jacobian matrix.

3.4. Multidomain decomposition in a distributed memory system

Three-dimensional problems are cumbersome to implement and a single processor cannot handle all the computational requirements since a refinement of the spatial and angular discretizations increases the required computational memory and time dramatically. Even for moderate cases the required memory surpasses the one of to-date available computers (*i.e.*, if a $30 \times 30 \times 30$ mesh and a S_{14} quadrature are used then 3.54 GB of RAM are needed to store the numbers in the Jacobian and their locations using a *double* precision).

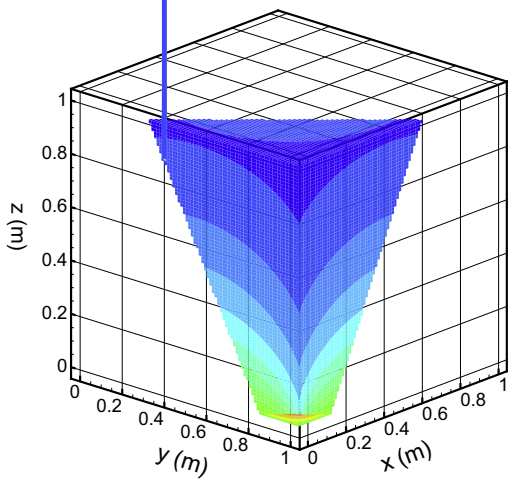

Massive parallel processors have become a useful alternative for 3D simulations, although pioneer work on the parallelization of the DOM has been applied to neutron transport problems [39–41] and only recently to thermal radiation problems [23,42–44]. In order to solve problems that require a fine mesh discretization, a domain decomposition parallelization strategy [23,43] is used with the aid of the MPJ-Express message passing libraries [45,46]. The overall domain is divided in subregions of equal dimension for which the RTE is solved using the Newton–Krylov method explained in the previous sections in order to take advantage of distributed memory systems. Two upstream intensities are to be communicated for a single direction, forming a $N(N+2)/2$ array per ghost cell, to maintain a flux limiter formulation reconstructing face intensities in the contiguous cell of the neighboring domain. A step scheme only requires a ghost cell in this formulation since for a first order approximation the intensities at the cell faces are equal to the intensities at the cell center. This fact is illustrated in Fig. 4 for which a single communication operation is shown for a specific direction. In summary, since there is six boundaries per domain there is a total of 12 operations (6 send and 6 receive), except for the domains that include the actual physical wall boundaries.

Another aspect is that neglecting some terms of the total Jacobian matrix due to the multidomain decomposition may influence the L_1-norm convergence. It will be shown that the values of the L_1-norm are small when compared to the differences introduced by spatial discretization, which is the main aspect in the inclusion of flux limiters. Communication between

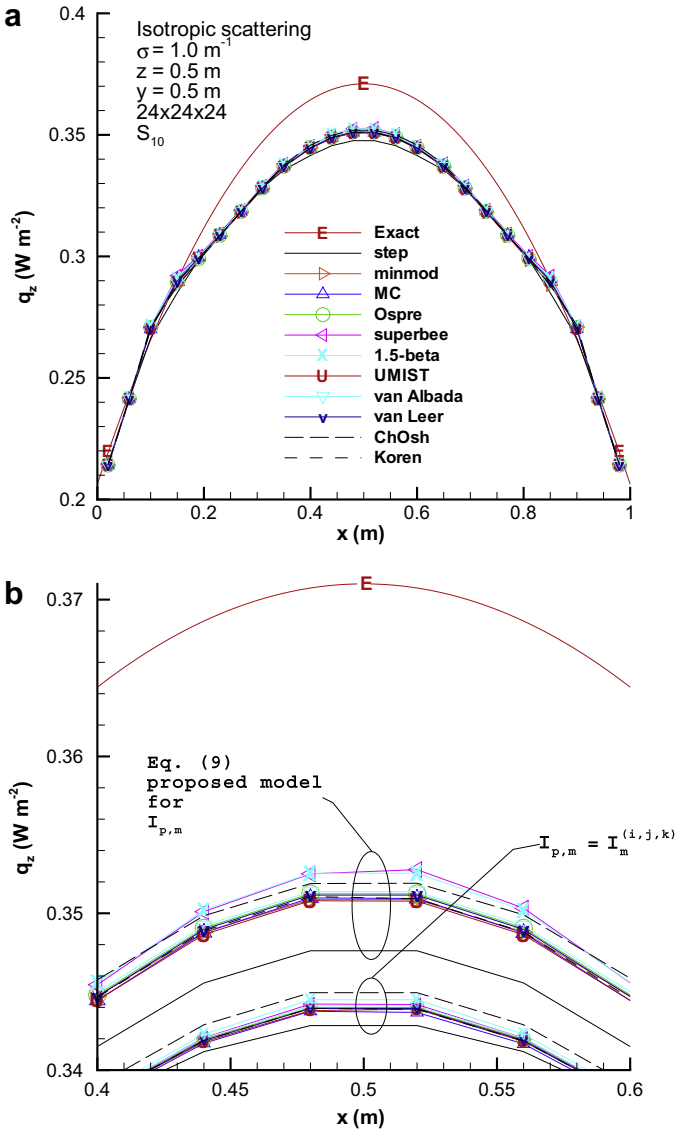

Fig. 11. Case 2: Heat flux in the z direction, q_z, using a $16 \times 16 \times 16$ mesh and a S_{10} quadrature for the isotropic scattering case for $y = z = 0.5$ m. (a) Entire x axis and (b) detailed view for $0.4 < x < 0.6$ using $I_{p,m} = I_m^{(i,j,k)}$ and the proposed model for $I_{p,m}$ from Eq. (9).

domains occurs right after each Newton iteration and therefore large discontinuities are not created between the processors due to several local iterations [23]. The downside is the increase in communication time since the passing elements are to be constructed, communicated and allocated in the memory of neighboring processors. This fact is analyzed in the last case of the results section showing the overall performance for different mesh sizes to balance accuracy with computational memory and time requirements.

In summary, the three sources of error introduced by the solution of the RTE using a DOM, finite volume discretization in a parallel multidomain decomposition procedure are: (i) numerical diffusion due to spatial discretization, (ii) ray effects due to angular discretization and (iii) maximum global convergence norm due to multidomain decomposition. To focus only on the effect of the flux limiters used in this study on the spatial discretization, the angular discretization is minimized by increasing the number of ordinate directions until results are independent of the order of the S_N quadrature. Also, it is shown that for a large number of Newton iterations the maximum convergence norm due to multidomain decomposition are several orders of magnitude smaller than the errors due to the spatial discretization scheme.

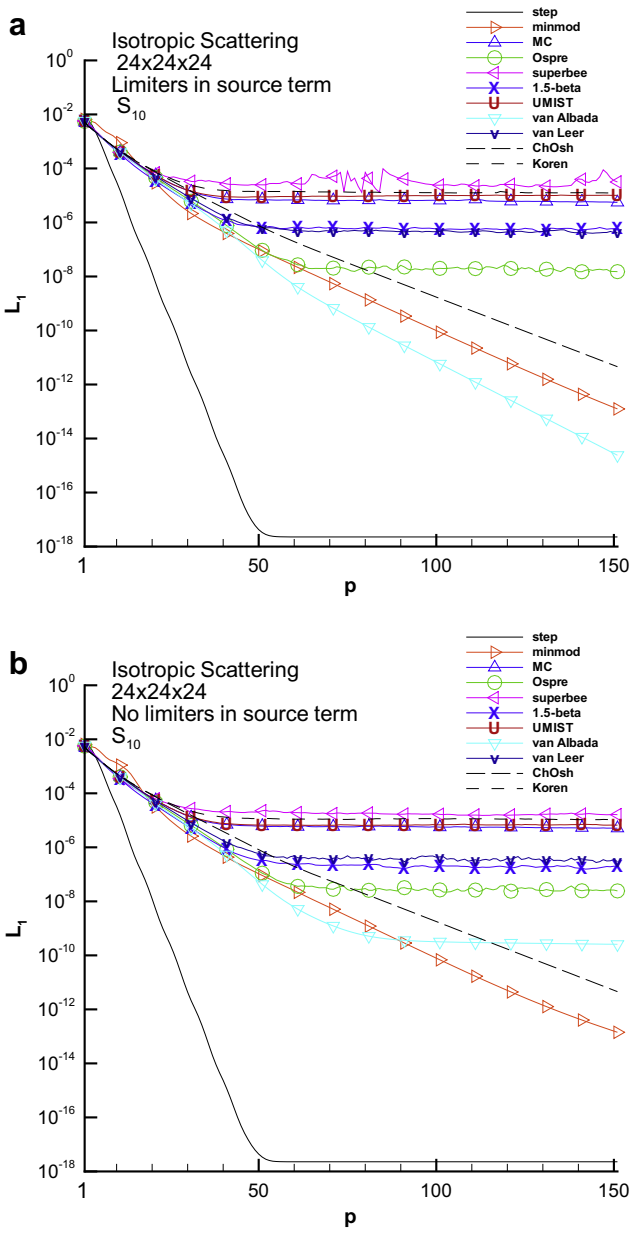

Fig. 12. Case 2: Convergence history of the step scheme and different limiters for the L_1 norm as a function of Newton iterations, p, using a GMRES(15) solution for a $24 \times 24 \times 24$ mesh for (a) limiters included in the source term and (b) limiters not included in the source term.

4. Results

In order to validate the procedure in 3D enclosures, three test cases are presented in which intensities are coupled to each other. Such cases are, (i) pure absorbing and emitting media in radiative equilibrium, (ii) pure isotropic scattering and anisotropic forward scattering media, and (iii) non-homogeneous, non-isothermal, absorbing, emitting and scattering media. Exact solutions are obtained using the analytical integral expressions given by Crosbie and Shrenker [24] for case (i) and for isotropic media in case (ii), whereas a Monte Carlo solution is given by Boulet et al. [25] for anisotropic forward scattering media in case (ii). Finally, case (iii) introduces the extension of flux limiters to non-homogeneous, non-isothermal media. Results are compared with those obtained for more refined spatial and angular discretization showing the performance of the limiters in more general situations.

4.1. Case 1: Absorbing-emitting media in radiative equilibrium

The first case consists of a pure absorbing-emitting cubical enclosure in radiative equilibrium. When radiative equilibrium is reached, the irradiation, G, is balanced with the blackbody emission from the medium, I_b at every location. In this

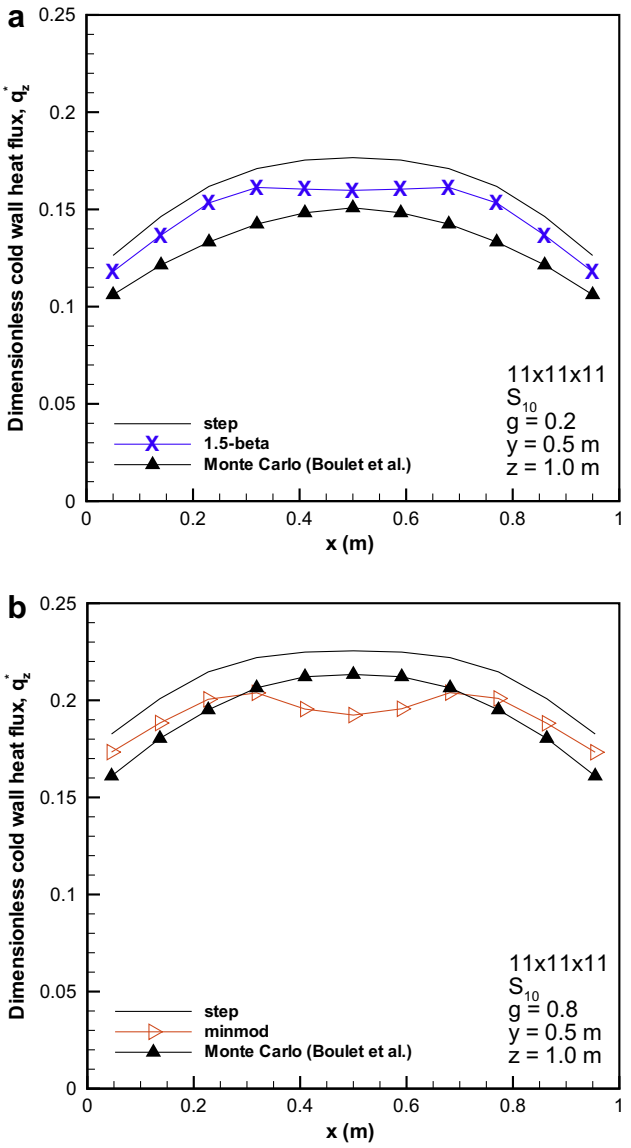

Fig. 13. Case 2: Comparison for the heat flux at the cold wall between the Monte Carlo, STEP, β-limiter and minmod schemes for pure forward scattering cases from [25] for a Henyey–Greenstein scattering function with (a) $g = 0.2$ and (b) $g = 0.8$.

limit for gray media, Eq. (3c) is identical to zero, $0 = k(4\pi I_b - G)$ and $I_b = G/(4\pi)$ hence I_b becomes a function of the average intensities at every cell which is directly imposed in the RTE to avoid operator splitting.

The test problem consists of a cubical enclosure of length $L_x = L_y = L_z = 1$ m with radiative black walls. The walls at locations $x = 1$ m, $y = 0$ m, $z = 0$ m have unitary emission ($I_{bw} = 1/\pi$), whereas the remaining are considered cold ($I_{bw} = 0$). The medium is homogeneous with a constant absorption coefficient of $k = 1$ m^{-1} in radiative equilibrium. To focus only on the effects of spatial discretization, a high-order S_{10} quadrature is employed to minimize ray-effects. In our calculations the final intensities remain unchanged beyond a S_{10} quadrature up to a 10^{-6} tolerance value.

Solutions to the same problem are also given by Fiveland [5] using a S_8 approximation for the step and diamond spatial discretizations, and by Larsen [47] using the zone method. For a fair evaluation of the exact solution the integral analytical expressions given by Crosbie and Schrenker [24] are solved numerically using Gauss–Seidel iterations on a $100 \times 100 \times 100$ mesh to ensure mesh independence up to a 10^{-8} tolerance.

Fig. 5 shows the emission along the medium in radiative equilibrium ($E = \pi I_b = G/4$) as a function of location calculated from (a) the exact integration of the RTE from [24], (b) step scheme and (c) superbee limiter on a $24 \times 24 \times 24$ mesh and S_{10} quadrature using 64 ($4 \times 4 \times 4$) processors. It can be seen that overall the DOM yields a good approximation to the exact solution with either a step scheme or a flux limiter for the presented meshes. In this case results using a superbee limiter

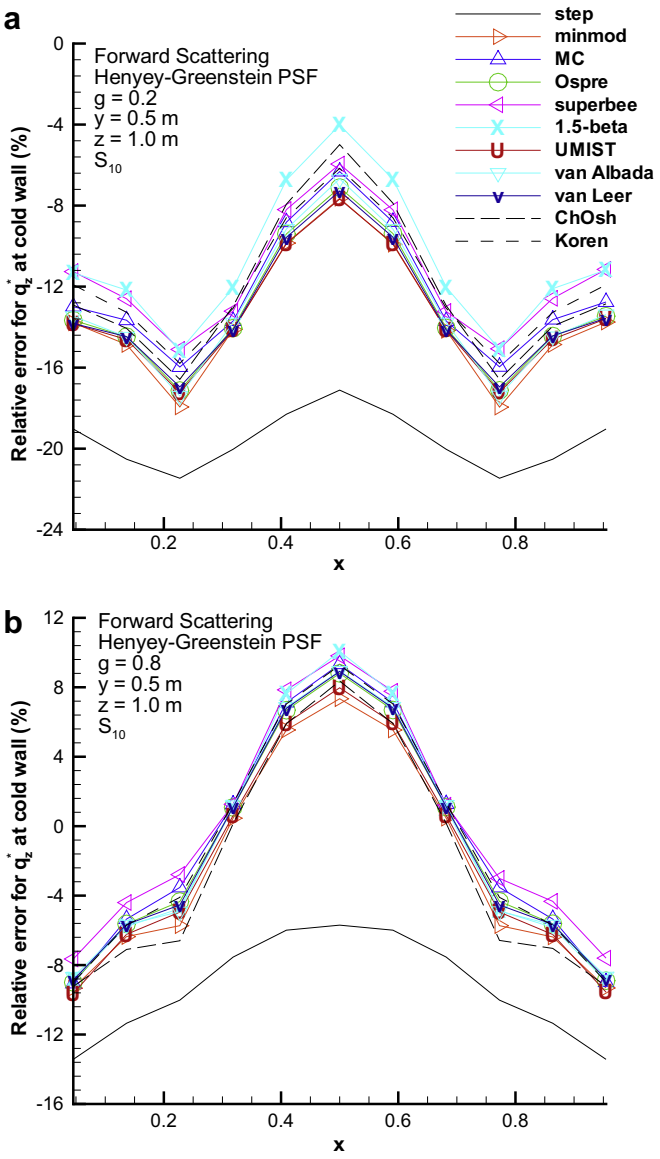

Fig. 14. Case 2: Relative errors compared to the cold wall heat flux obtained with the Monte Carlo method [25] for different flux limiters for the case in Fig. 13 for (a) $g = 0.2$ and (b) $g = 0.8$.

are shown since it posses the most anti-diffusive characteristic. A more detailed view of the 3D results is shown in Fig. 6 in which the emission, E, is plotted as a function of location in the $z = 0.5$ m plane for three different locations in the y direction and two different mesh sizes of (a) $16 \times 16 \times 16$ (8 processors) and (b) $24 \times 24 \times 24$ (64 processors).

Mesh convergence is shown in Fig. 7 by plotting the norm defined from Eq. (17) for the average emission error along the whole domain. It is seen that all limiters show a convergence rate higher than the 1st order step scheme, but they never reach a 2nd order rate and for this test case the order of convergence is between 1.6 and 1.7 for all limiters. Balsara [17] found that the analogous 2D methods only reached their stated accuracy on 200×200 zones or more. On 100×100 zones or less, he found that the order of accuracy was around 1.7, too. Thus showing that the proposed methods only reach their theoretical accuracy from below. Since the present authors cannot run simulations with $200 \times 200 \times 200$ or more zones, they are not in a position to verify the full theoretical accuracy of the schemes in the present work. The two main reasons for not achieving 2nd order convergence may be explained by the fact that the present discretization schemes are not truly multi-dimensional and also due to the 1st order discretization at the boundaries. Overall, any flux limiter represents an improvement in the spatial discretization when compared to a first order step scheme, but it is difficult to select an ideal limiter for this case since they are bounded to the same TVD region and the differences between them are of no more than 0.5%.

In order to balance computational time with total accuracy, the L_1 norm defined in Eq. (16) is shown in Fig. 8 for two mesh sizes, $16 \times 16 \times 16$ and $24 \times 24 \times 24$, as a function of the number of Newton iterations. Most limiters converge to tolerance values ranging from $L_1 = 10^{-4}$ to 10^{-6} with the exception of the Chakravarty-Osher and the van Albada limiters which have a smooth convergence and smaller tolerances, therefore variations are too small to affect the final answer. Other limiters present oscillations in the convergence history of L_1 as the following iterations have to compensate for the excess in the anti-diffusion terms, except for the minmod limiter for which convergence is achieved faster on a coarser mesh. Increasing the number of cells, thus decreasing the cell width, smoothes the convergence history of L_1, although more iterations are needed to achieve a final convergence characteristic except for the Chakravarty-Osher and van Albada limiters which converge faster on a more refined mesh than on a coarser one. Therefore, the number of iterations to obtain a final answer has to be considered for the overall performance of the flux limiters when compared to the step scheme which require a much fewer number of iterations to reach small variations. In general, a larger number of iterations are required for more refined meshes, but this penalty is compensated with a higher level of accuracy.

Additionally, in order to guarantee that the errors shown in this study are mainly due to the spatial discretization the emission along the medium using a superbee limiter on a $16 \times 16 \times 16$ mesh for the $y = 0.5$ m and $z = 0.5$ m line is shown in Fig. 9 as a function of (a) the number of Newton iterations, p, and (b) the S_N quadrature order. As it is seen in Fig. 9 for a large number of Newton iterations and ordinate directions, results become nearly independent of these two parameters. Therefore, variations due to angular discretization and the number of Newton iterations are several orders of magnitude smaller than those introduced by spatial discretization.

4.2. Case 2: Isotropic and forward anisotropic pure scattering media

A second test case considers pure scattering in a cold medium. The first part presents an isotropic scattering case and for the second part a forward anisotropic scattering problem with constant phase scattering function. The inclusion of flux

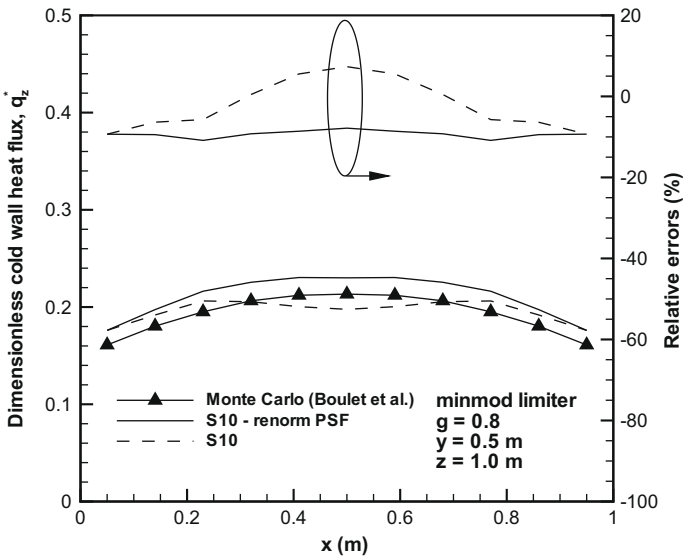

Fig. 15. Case 2: Comparison for the heat flux at the cold wall between the Monte Carlo method from [25] and the minmod limiter for a pure forward scattering case for a Henyey–Greenstein scattering function of $g = 0.8$ using renormalization of the PSF.

limiters in the source (in-scattering) term of the RTE as suggested in the present work, is discussed. For both problems a cubical enclosure of $L = 1$ m and a constant scattering coefficient of $\sigma = 1$ m^{-1} is exposed to a hot wall with unitary emission ($I_{bw} = 1/\pi$) at $z = 0$ while the other walls are considered cold ($I_{bw} = 0$).

Exact results from the integration of the RTE from Ref. [24] are calculated on a $80 \times 80 \times 80$ mesh. The same problem has been solved by Trivic and Amon [48] using a combined Monte Carlo and zone method. For the forward anisotropic scattering cases results from the work of Boulet et al. [25] using a Monte Carlo solution are presented for the same configuration using the Henyey–Greenstein approximation [31], with average PSF cosines of $g = 0.2$ and 0.8. These cases are compared with a S_{10} DOM solution using the flux limiters proposed in this work. As it will be shown, the limiters in the source term must be accompanied with proper renormalization of the PSF to avoid non-physical results. On the other hand, total exclusion of the limiters from the source term leads to larger errors in the calculation of the heat flux. The DOM is known for reduced accuracy in scattering atmospheres as more directions are involved in the calculation of a single intensity, even though the inclusion of flux limiters does result in certain improvement.

Results obtained for an isotropic medium case is shown in Fig. 10 for the irradiation, G, as a function of location calculated from (a) the exact integration of the RTE from [24] using a $80 \times 80 \times 80$ mesh, (b) step scheme and (c) superbee limiter on a $24 \times 24 \times 24$ mesh using 64 ($4 \times 4 \times 4$) processors. A detailed plot for the heat flux in the z direction, q_z, is shown in Fig. 11 as a function of the x coordinate at location $y = 0.5$ m and $z = 0.5$ m on a $24 \times 24 \times 24$ mesh. For this case larger differences arises at the center of the domain, whereas at the walls all schemes show similar results. A more detailed view of the center of the domain is presented in Fig. 11(b) in which the superbee and the 1.5-β limiters show a similar performance overcoming

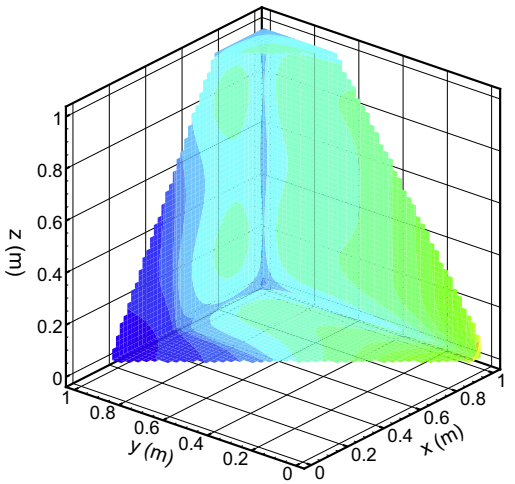

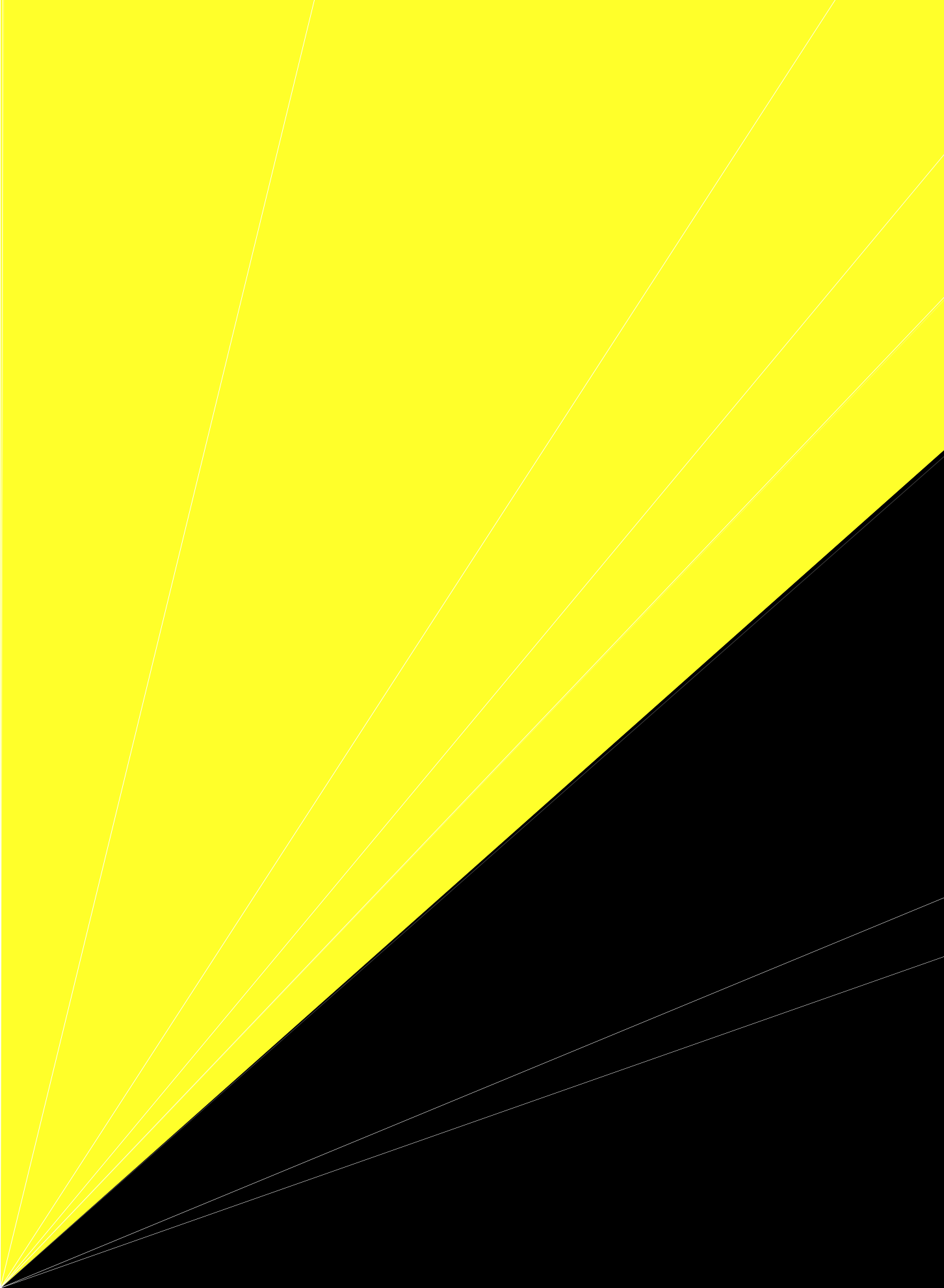

4.3. Case 3: Non-homogeneous, non-isothermal, absorbing, emitting and scattering media

The last case presents a 3D non-homogeneous, non-isothermal and scattering medium in a known temperature field for which exact analytical solutions do not exist. The motivation for introducing this case is that most practical problems in radiative transport include all these characteristics therefore a general formulation must be pursued. For this case, mesh independence and the required CPU memory and times are introduced and discussed to understand the performance of each of the limiters and the step scheme to balance accuracy and computational costs. The problem consists of a cubical enclosure of $L = 1$ m with variable radiative properties governed by the following expression,

$$R = R_o \times \frac{2\sqrt{(x-x_0)^2 + (y-y_0)^2 + (z-z_0)^2}}{\sqrt{3}L} \tag{18}$$

where R represents $\beta,\ \sigma,\ k$ and I_b from Eq. (1) and $x_0 = y_0 = z_0 = 0.5$ m represent the location of the center of the whole domain. Additionally, $I_{bo} = 0$ for $x < 0.5$ m introducing a sharp variation of the temperature in the middle of the domain. The Henyey–Greenstein scattering phase function is employed to model scattering characteristics and a constant value of $g = 0.7$ is assigned to the entire domain. The boundary conditions at the black walls are established such that only the plane at $y = 0$

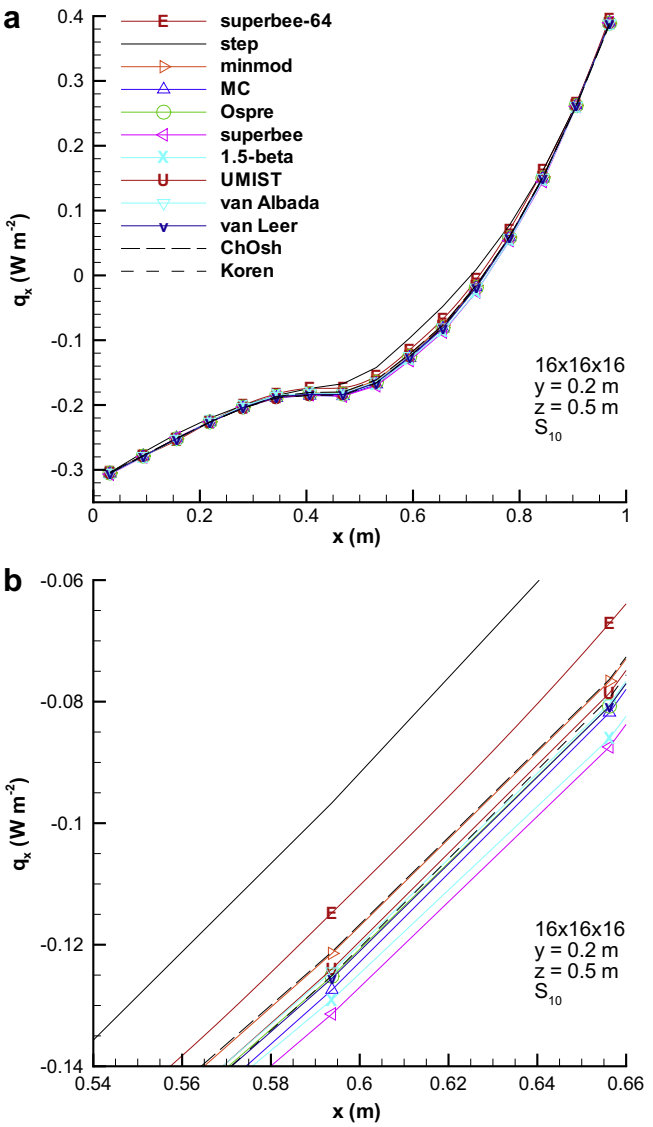

Fig. 18. Case 3: Heat flux in the x direction, q_x, using a $16 \times 16 \times 16$ mesh and a S_{10} quadrature for the non-homogeneous, non-isothermal case at location $y = 0.2$ m and $z = 0.5$ m. (a) Entire x axis, (b) detailed view for $0.54 < x < 0.6$ showing the differences between the limiters and the step scheme.

has unitary emission ($I_{bw} = 1/\pi$), whereas the rest are considered cold ($I_{bw} = 0$). Therefore, the medium is considered non-homogeneous and non-isothermal due to the spatial variations of the radiative properties and the blackbody function while keeping a symmetric characteristic with respect to the z-axis.

The values of $\beta_o = 1\ \mathrm{m}^{-1}$, $\sigma_o = 0.5\ \mathrm{m}^{-1}$, $k_o = 0.5\ \mathrm{m}^{-1}$ and $I_{bo} = 3/\pi$ are considered for the medium properties. Solutions using a superbee limiter on a $64 \times 64 \times 64$ mesh using $8 \times 8 \times 8$ processors is presented in Fig. 16(a). Results are also presented in the same figure for a $16 \times 16 \times 16$ mesh ($4 \times 4 \times 4$ processors) using (b) the step scheme and (c) the superbee limiter. The differences between the two schemes are noticeable for this mesh configuration and it is clear that the inclusion of a flux limiter can be easily extended to a more general case.

From case 1, the flux limiters mesh convergence rate is between a first and a second order formulation. This fact can be extended to the present case for the heat flux in the x direction, q_x. Fig. 17 presents the values of q_x for half of the domain, due to symmetry conditions with respect to the z-axis, for (a) the superbee scheme using a $64 \times 64 \times 64$ mesh, (b) the step scheme using a $16 \times 16 \times 16$ mesh and (c) the superbee limiter in a $16 \times 16 \times 16$ mesh. It is seen that even for a low resolution mesh the superbee limiter shows a closer representation of the heat flux field when compared to results from a more refined mesh. A more detailed plot of the heat flux is presented at location $y = 0.2$ m and $z = 0.5$ in Fig. 18 showing a comparison between the different limiters with results from the superbee scheme using a more refined mesh. Fig. 18(a) shows

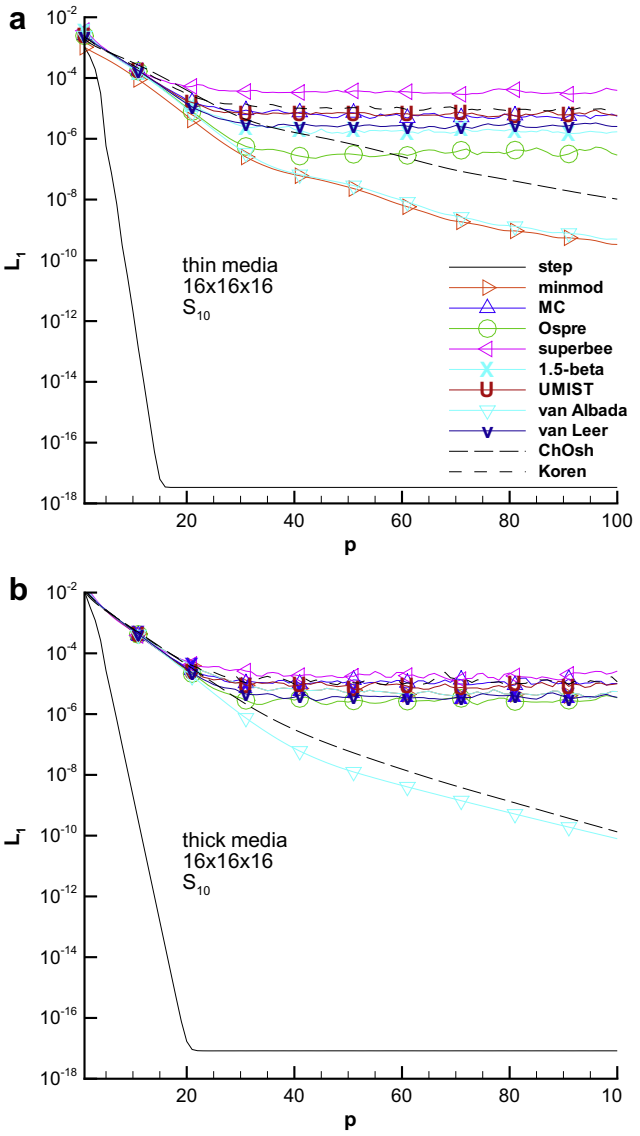

Fig. 19. Case 3: Convergence history of the step scheme and different limiters for the L_1 norm as a function of Newton iterations, p, using a GMRES(15) solution for a $16 \times 16 \times 16$ mesh for (a) a optically thin medium, $\beta_0 = 1\ \mathrm{m}^{-1}$ and (b) a optically thick medium $\beta_0 = 10\ \mathrm{m}^{-1}$. In both cases $k_0 = \sigma_0 = 0.5 \times \beta_0$.

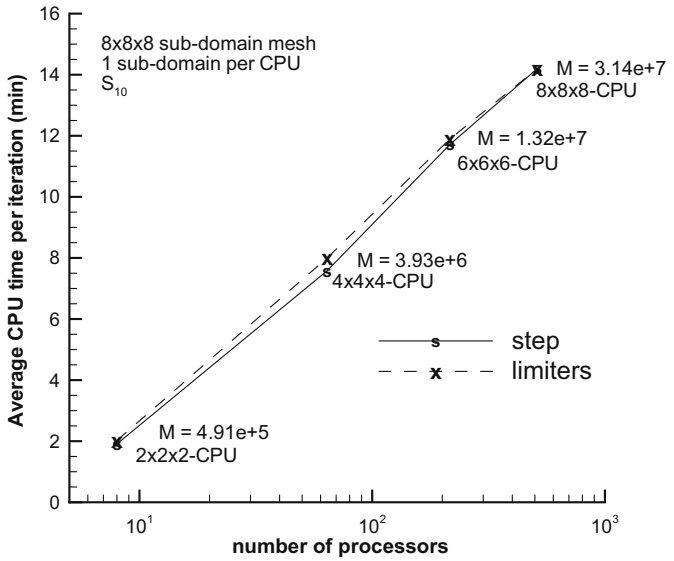

Fig. 20. Case 3: Typical average computational times per Newton iteration as a function of the number of processors on a regular $8 \times 8 \times 8$ mesh per subdomain and 1 CPU per subdomain. Results are plotted for the step scheme and the different limiters used in this stud.

that results for q_x are very similar near the boundaries, whereas differences will arise near the center of the domain. Fig. 18(b) shows a more detailed plot for locations $0.54 < x < 0.6$. It is seen that results from the Chakravarty-Osher and minmod limiters are closer to the answer provided by a more refined mesh using the superbee scheme and contrary to the previous cases, the superbee and 1.5-β limiters are outperformed by all other limiters underpredicting the heat flux in that location. Another aspect for this case is the Newton convergence of L_1 as presented in Fig. 19 for (a) a thin medium, $\beta_o = 1\ \mathrm{m}^{-1}$ and (b) a thick medium $\beta_o = 10\ \mathrm{m}^{-1}$. In both cases the convergence pattern of L_1 show a similar behavior for all limiters except for the minmod limiter and the step scheme. In the case of the minmod limiter as the medium becomes thicker faster convergence is achieved. These results suggest that for both cases the dominant intensities ratios are close to unity explaining the change in the convergence history of the minmod limiter.

Finally, typical computational times are presented for a single Newton iteration in a parallel multidomain solution. CPU times are extremely dependent on external factors such as loading and hardware characteristics therefore fair average values are taken without considering the times that fall far away from the averages. Comparing CPU times for each limiter is not noticeable since a general formulation will allow for the maximum number of non-zero elements of the Jacobian to be stored and in some case zero derivatives will also be carried. Only a noticeable difference is found when CPU times are compared to the ones required for the step scheme. Fig. 20 shows representative times for a single Newton iteration including communication between subdomains. These times are given when a subdomain of $8 \times 8 \times 8$ and a S_{10} quadrature is used in multiple processor arrays. The difference between the step scheme and all other limiters is due to the fact that the storing of the Jacobian matrix and Newton–Krylov iterations are less intensive operations for the step scheme as the stencil is more compact. This difference is attenuated as the number of processors is increased and communication times become more relevant for the overall CPU time. The number of total unknowns, M, are shown for each case as well. Balancing CPU times per iteration in Fig. 20 with the number of iterations needed for convergence in Fig. 19(a) and accuracy in Fig. 18 demonstrates that the inclusion of flux limiters signifies an improvement of the overall solution of the RTE, especially when coarser meshes are to be employed.

5. Conclusions

The application of flux limiters to the discrete ordinates method (DOM) for radiative transfer calculations is discussed and analyzed for 3D enclosures. In all cases, the use of flux limiter has proven to be a superior approach in solving the RTE when compared to the step scheme. Overall, most limiters have approximately the same performance, but the superbee limiter is slightly more accurate for moderate pure absorbing-emitting and isotropic scattering media. For anisotropic scattering media, this is not always the case as the 1.5-β limiter shows a better performance as the intensity is influenced by the in-scattering term so a limiter that has the largest anti-diffusive characteristic is not recommended. Mesh convergence rate using flux limiters is shown to be in between a first order and second order spatial accuracy, with an exponential ratio between 1.6 and 1.7 for all limiters on meshes that fall below $100 \times 100 \times 100$. Including flux limiters in the source term may lead to non-physical results in forward anisotropic scattering media. On the other hand,

neglecting the flux limiter values in the in-scattering terms leads to results close to pure transmission cases as the forward peak is usually overestimated in the DOM. Therefore, renormalization of the forward peak in the PSF and inclusion of flux limiters become a better alternative for forward scattering cases. For non-homogeneous, non-isothermal, scattering, emitting and absorbing domains the formulation is easily extended and the inclusion of flux limiters outperforms the step scheme when accuracy is balanced with CPU times and the number of Newton iterations needed to reach convergence. Finally, the use of flux limiters in the DOM represents an improvement over the step scheme for all the cases shown in this study.

Acknowledgments

This research is supported by the National Science Foundation under Grant No. CTS-034811. The authors would like to acknowledge the Center of Computational Research (CCR) of SUNY at Buffalo for the use of their facilities to run the presented calculations. The first author would like to acknowledge Dr. Mark Carrara from Los Alamos National Laboratories (LANL) for his mentoring during the summer of 2007 at the X-4 Division SS-Group at LANL.

Appendix A. Definition of the flux limiters used in the present work

A.1. Symmetric limiters, $\frac{\Psi(r)}{r} = \Psi\left(\frac{1}{r}\right)$

minmod

$$\Psi(r) = max[0, min(1, r)] \tag{A.1a}$$

monotonized central MC (van Leer),

$$\Psi(r) = max\left[0, min\left(2r, \frac{1+r}{2}, 2\right)\right] \tag{A.1b}$$

Ospre (Waterson and Deconinck),

$$\Psi(r) = \frac{1.5(r^2+r)}{r^2+r+1} \tag{A.1c}$$

superbee (Roe),

$$\Psi(r) = max[0, min(2r, 1), min(r, 2)] \tag{A.1d}$$

Sweby's β-limiters $(1 \leqslant \beta \leqslant 2)$

$$\Psi(r) = max[0, min(\beta r, 1), min(r, \beta)] \tag{A.1e}$$

UMIST (Lien and Leschziner),

$$\Psi(r) = max[0, min(2r, 0.25 + 0.75r, 0.75 + 0.25r, 2)] \tag{A.1f}$$

van Albada,

$$\Psi(r) = \frac{r^2+r}{r^2+1} \tag{A.1g}$$

van Leer,

$$\Psi(r) = \frac{r+|r|}{1+r} \tag{A.1h}$$

A.2. Non-symmetric limiters, $\frac{\Psi(r)}{r} \neq \Psi\left(\frac{1}{r}\right)$

Chakravarthy-Osher $(1 \leqslant \beta \leqslant 2)$

$$\Psi(r) = max[0, min(r, \beta)] \tag{A.2a}$$

Koren

$$\Psi(r) = max\left[0, min\left(2r, \frac{1+2r}{3}, 2\right)\right] \tag{A.2b}$$

Appendix B. First order partial derivatives of the error function in the *x*-direction

$$\frac{\partial E_m^{(i,j,k)}}{\partial I_n^{(i\pm2,j,k)}} = H(\pm\vec{s}_m\cdot\vec{e}_x)\left(H(-\vec{s}_m\cdot\vec{s}_n)\left[-k\frac{\partial I_b^{(i,j,k)}}{\partial I_n^{(i\pm2,j,k)}}-\frac{\sigma}{4\pi}w_n\Phi_{nm}\frac{\partial I_{p,n}^{(i,j,k)}}{\partial I_n^{(i\pm2,j,k)}}\right]\right)+H(\mp\vec{s}_m\cdot\vec{e}_x)$$
$$\times\left(H(\vec{s}_m\cdot\vec{s}_n)\left[\delta_{mn}\frac{|\xi_m|}{\Delta x}\left(-\frac{\partial\Psi_m^{(i\pm1)}}{\partial I_n^{(i\pm2,j,k)}}\frac{\left(I_m^{(i\pm1,j,k)}-I_m^{(i\pm2,j,k)}\right)}{2}+\frac{\Psi_m^{(i\pm1)}}{2}\right)\right.\right.$$
$$\left.\left.+\delta_{mn}\beta\frac{\partial I_{p,m}^{(i,j,k)}}{\partial I_n^{(i\pm2,j,k)}}-k\frac{\partial I_b^{(i,j,k)}}{\partial I_n^{(i\pm2,j,k)}}-\frac{\sigma}{4\pi}w_n\Phi_{nm}\frac{\partial I_{p,n}^{(i,j,k)}}{\partial I_n^{(i\pm2,j,k)}}\right]\right) \tag{B.1a}$$

$$\frac{\partial E_m^{(i,j,k)}}{\partial I_n^{(i\pm1,j,k)}} = H(\pm\vec{s}_m\cdot\vec{e}_x)\left(H(\vec{s}_m\cdot\vec{s}_n)\left[\delta_{mn}\frac{|\xi_m|}{\Delta x}\left(-\frac{\partial\Psi_m^{(i)}}{\partial I_n^{(i\pm1,j,k)}}\frac{\left(I_m^{(i,j,k)}-I_m^{(i\pm1,j,k)}\right)}{2}\right)\right]+H(-\vec{s}_m\cdot\vec{s}_n)\left[-k\frac{\partial I_b^{(i,j,k)}}{\partial I_n^{(i\pm1,j,k)}}-\frac{\sigma}{4\pi}w_n\Phi_{nm}\frac{\partial I_{p,n}^{(i,j,k)}}{\partial I_n^{(i\pm1,j,k)}}\right]\right)$$
$$+H(\mp\vec{s}_m\cdot\vec{e}_x)H(\vec{s}_m\cdot\vec{s}_n)\left[\delta_{mn}\frac{|\xi_m|}{\Delta x}\left(-1+\frac{\partial\Psi_m^{i}}{\partial I_n^{(i\pm1,j,k)}}\frac{\left(I_m^{(i,j,k)}-I_m^{(i\pm1,j,k)}\right)}{2}-\frac{\Psi_m^{i}}{2}-\frac{\partial\Psi_m^{(i\pm1)}}{\partial I_n^{(i\pm1,j,k)}}\frac{\left(I_m^{(i\pm1,j,k)}-I_m^{(i\pm2,j,k)}\right)}{2}+\frac{\Psi_m^{(i\pm1)}}{2}\right)\right.$$
$$\left.+\delta_{mn}\beta\frac{\partial I_{p,m}^{(i,j,k)}}{\partial I_n^{(i\pm1,j,k)}}-k\frac{\partial I_b^{(i,j,k)}}{\partial I_n^{(i\pm1,j,k)}}-\frac{\sigma}{4\pi}w_n\Phi_{nm}\frac{\partial I_{p,n}^{(i,j,k)}}{\partial I_n^{(i\pm1,j,k)}}\right] \tag{B.1b}$$

$$\frac{\partial E_m^{(i,j,k)}}{\partial I_n^{(i,j,k)}} = H(\pm\vec{s}_m\cdot\vec{e}_x)\left(\delta_{mn}\frac{\xi_m}{\Delta x}\left[1+\frac{\Psi_m^{(i,j,k)}}{2}+\frac{\partial\Psi_m^{(i,j,k)}}{\partial I_n^{(i,j,k)}}\frac{\left(I_m^{(i,j,k)}-I_m^{(i\mp1,j,k)}\right)}{2}-\frac{\partial\Psi_m^{(i\mp1,j,k)}}{\partial I_n^{(i,j,k)}}\frac{\left(I_m^{(i\mp1,j,k)}-I_m^{(i\mp2,j,k)}\right)}{2}\right]\right.$$
$$+\delta_{mn}\frac{\eta_m}{\Delta y}\left[1+\frac{\Psi_m^{(i,j,k)}}{2}+\frac{\partial\Psi_m^{(i,j,k)}}{\partial I_n^{(i,j,k)}}\frac{\left(I_m^{(i,j,k)}-I_m^{(i,j\mp1,k)}\right)}{2}-\frac{\partial\Psi_m^{(i,j\mp1,k)}}{\partial I_n^{(i,j,k)}}\frac{\left(I_m^{(i,j\mp1,k)}-I_m^{(i,j\mp2,k)}\right)}{2}\right]$$
$$+\delta_{mn}\frac{\mu_m}{\Delta z}\left[1+\frac{\Psi_m^{(i,j,k)}}{2}+\frac{\partial\Psi_m^{(i,j,k)}}{\partial I_n^{(i,j,k)}}\frac{\left(I_m^{(i,j,k)}-I_m^{(i,j,k\mp1)}\right)}{2}-\frac{\partial\Psi_m^{(i,j,k\mp1)}}{\partial I_n^{(i,j,k)}}\frac{\left(I_m^{(i,j,k\mp1)}-I_m^{(i,j,k\mp2)}\right)}{2}\right]$$
$$\left.+\delta_{mn}\beta\frac{\partial I_{p,m}^{(i,j,k)}}{\partial I_n^{(i,j,k)}}-k\frac{\partial I_b^{(i,j,k)}}{\partial I_n^{(i,j,k)}}-\frac{\sigma}{4\pi}w_n\Phi_{nm}\frac{\partial I_{p,m}^{(i,j,k)}}{\partial I_n^{(i,j,k)}}\right) \tag{B.1c}$$

where H is the discrete Heaviside function; δ the Kronecker delta function; $\vec{e}_x$ is the Cartesian x-unitary vector.

References

[1] S. Chandrasekhar, Radiative Transfer, Dover, New York, NY, 1960.
[2] M. Modest, Radiative Heat Transfer, second ed., Academic Press, Elsevier Science, San Diego, CA, 2003.
[3] K. Lathrop, B. Carlson, Transport theory, the method of discrete ordinates, Tech. Rep. LA-3251-MS, Los Alamos Scientific Laboratory, Los Alamos, NM, 1965.
[4] K. Lathrop, B. Carlson, Numerical solution of the Boltzmann transport equation, J. Comput. Phys. 1 (1966) 173–197.
[5] W. Fiveland, Three-dimensional radiative heat transfer solutions by the discrete ordinates method, J. Thermophys. Heat Trans. 2 (1988) 309–316.
[6] W. Fiveland, A. Jamaluddin, Three-dimensional spectral radiative heat transfer solutions by the discrete ordinates method, J. Thermophys. Heat Trans. 5 (1991) 335–339.
[7] J. Chai, H. Lee, S. Patankar, Ray effect and numerical scattering in the discrete ordinates method, Numer. Heat Trans. Pt. B: Fund. 24 (1993) 373–389.
[8] P. Coelho, The role of ray effects and false scattering on the accuracy of the standard and modified discrete ordinates methods, J. Quant. Spec. Rad. Trans. 73 (2002) 231–238.
[9] J. Jessee, W. Fiveland, Bounded, high-resolution differencing schemes applied to the discrete ordinate method, J. Thermophys. Heat Trans. 11 (1997) 540–548.
[10] M. Ramankutty, A. Crosbie, Modified discrete ordinates solution of radiative transfer in two-dimensional rectangular enclosures, J. Quant. Spec. Rad. Trans. 57 (1997) 107–140.
[11] D. Mihalas, R. Klein, On the solution of the time-dependent inertial-frame equation of radiative transfer in moving media to o(v/c), J. Comput. Phys. 46 (1982) 97–137.
[12] I. Ayranci, N. Selçuk, MOL solution of DOM for transient radiative transfer in 3-D scattering media, J. Quant. Spec. Rad. Trans. 84 (2004) 409–422.
[13] A. Harten, High resolution schemes for hyperbolic conservation laws, J. Comput. Phys. 49 (1983) 357–393.
[14] P. Sweby, High resolution schemes using flux limiters for hyperbolic conservation laws, SIAM J. Numer. Anal. 21 (1984) 995–1011.
[15] B. van Leer, Towards the ultimate conservative difference scheme. II. Monotonicity and conservation combined in a second-order scheme, J. Comput. Phys. 14 (1974) 361–370.
[16] B. van Leer, Towards the ultimate conservative difference scheme. V. A second-order sequel to Godunov's method, J. Comput. Phys. 32 (1979) 101–136.
[17] D. Balsara, Fast and accurate discrete ordinates methods for multidimensional radiative transfer. Part I: Basic methods, J. Quant. Spec. Rad. Trans. 69 (2001) 671–707.
[18] P. Roe, D. Sidilkover, Optimum positive linear schemes for advection in two and three dimensions, SIAM J. Numer. Anal. 29 (1992) 1542–1568.
[19] P. Coelho, Bounded skew high-order resolution schemes for the discrete ordinates method, J. Comput. Phys. 175 (2002) 412–437.

[20] P. Coelho, A comparison of spatial discretization schemes for differential solution methods of the radiative transfer equation, J. Quant. Spec. Rad. Trans. 109 (2008) 189–200.
[21] Y. Saad, M. Schultz, GMRES: a generalized minimal residual algorithm for solving non-symmetric linear systems, SIAM J. Sci. Stat. Comput. 7 (1986) 856–869.
[22] W. Gropp, E. Lusk, A. Skjellum, Using MPI Portable Parallel Programming with the Message-Passing Interface, second ed., The MIT Press, London, England, 1999.
[23] P. Gonçalves, P. Coelho, Parallelization of the discrete ordinates method, Numer. Heat Trans. Pt. B: Fund. 32 (1997) 151–173.
[24] A. Crosbie, R. Schrenker, Exact expressions for radiative transfer in a three-dimensional rectangular geometry, J. Quant. Spec. Rad. Trans. 28 (1982) 507–526.
[25] P. Boulet, A. Collin, J. Consalvi, On the finite volume method and the discrete ordinates method regarding radiative heat transfer in acute forward anisotropic scattering media, J. Quant. Spec. Rad. Trans. 104 (2007) 460–473.
[26] J. Howell, Application of Monte Carlo to Heat Transfer Problems, Advances in Heat Transfer, vol. 5, Academic Press, New York, NY, 1968.
[27] H. Hottel, A. Sarofim, Radiative Transfer, McGraw-Hill Inc., New York, NY, 1967.
[28] W. Fiveland, The selection of discrete ordinate quadrature sets for anisotropic scattering. fundamentals of radiation heat transfer, ASME, HTD 160 (1991) 89.
[29] J. Joseph, W. Wiscombe, J. Weinman, The delta-Eddington approximation for radiative flux transfer, J. Atmos. Sci. 33 (1976) 2452–2459.
[30] W. Wiscombe, On initialization error and flux conservation in the doubling method, J. Quant. Spec. Rad. Trans. 18 (1976) 637–658.
[31] L. Henyey, J. Greenstein, Diffuse radiation in the galaxy, Astrophys. J. 93 (1941) 70–83.
[32] C. Hirsch, Numerical Computation of Internal and External Flows, Computational Methods for Inviscid and Viscous Flows, vol. 2, John Wiley & Sons, Chichester, England, 1990.
[33] W. Fiveland, J. Jessee, Acceleration schemes for the discrete ordinates method, J. Thermophys. Heat Trans. 10 (1996) 445–451.
[34] S. Halliday, B.O. Heimsund, Matrix Toolkits for Java (MTJ), 2006. <http://code.google.com/p/matrix-toolkits-java/>.
[35] BLAS – Basic Linear Algebra Subprograms, 1979. <http://www.netlib.org/blas>.
[36] LAPACK – Linear Algebra Package, 1992. <http://www.netlib.org/lapack>.
[37] Y. Saad, Iterative Methods for Sparse Linear Systems, second ed., SIAM, Philadelphia, PA, 2003.
[38] D. Knoll, D. Keyes, Jacobian-free Newton–Krylov methods: a survey of approaches and applications, J. Comput. Phys. 193 (2004) 357–397.
[39] R. Mattis, A. Haghihat, Domain decomposition of a two-dimensional S_N transport method, Nucl. Sci. Eng. 108 (1992) 267–277.
[40] U. Hannebutte, Lewis, A massively parallel discrete ordinates method response matrix method for neutron transport, Nucl. Sci. Eng. 111 (1992) 46–56.
[41] K. Kock, R. Baker, R. Alcouffe, Solution of the first-order form of the 3D discrete ordinates equation on a massively parallel processor, Trans. Am. Nucl. Soc. 65 (1992) 198–199.
[42] L. Gritzo, R. Skocypec, T. Tong, The use of high-performance computing to solve participating media radiative heat transfer problems results of an NSF workshop, Tech. Rep. SAND95-0225, Sandia Nat Lab, 1995.
[43] O. Yldz, H. Bedir, A parallel solution to the radiative transport in three-dimensional participating media, Numer. Heat Trans. Pt. B: Fund. 50 (2006) 79–95.
[44] A. Chandy, D. Glaze, S. Frankel, Parallelizing the discrete ordinates method (DOM) for three-dimensional radiative heat transfer calculations using a priority queuing technique, Numer. Heat Trans. Pt. B: Fund. 52 (2007) 33–49.
[45] B. Carpenter, V. Getov, G. Judd, A. Skjellum, G. Fox, MPJ: MPI-like message passing for Java, Concurrency: Pract. Exper. 12 (2000) 1019–1038.
[46] M. Baker, B. Carpenter, A. Shafi, MPJ Express Project, 2009. <http://www.mpj-express.org/>.
[47] M. Larsen, Exchange factor method and alternative zonal formulation for analysis of radiating enclosures containing participating media, Ph.D. Dissertation, University of Texas, Austin, TX, 1983.
[48] D. Trivic, C. Amon, Modeling the 3D radiation of anisotropically scattering media by two different numerical methods, Int. J. Heat Mass Trans. 51 (2008) 2711–2732.